TU Delft

Delft University of Technology

Document Version
Final published version

Licence
Dutch Copyright Act (Article 25fa)

Citation (APA)
Xiao, Y., Deng, Z., Zhou, S., Chang, Z., Mao, J., Shen, Z., Wang, W., & Tan, S. (2026). Modeling dynamic responses of three-dimensional high-speed train-ballasted track-subgrade coupled system subjected to spatial differential subgrade settlement. *Transportation Geotechnics*, *59*, Article 101965. https://doi.org/10.1016/j.trgeo.2026.101965

Important note
To cite this publication, please use the final published version (if applicable).
Please check the document version above.

Copyright
In case the licence states “Dutch Copyright Act (Article 25fa)”, this publication was made available Green Open Access via the TU Delft Institutional Repository pursuant to Dutch Copyright Act (Article 25fa, the Taverne amendment). This provision does not affect copyright ownership.
Unless copyright is transferred by contract or statute, it remains with the copyright holder.

Sharing and reuse
Other than for strictly personal use, it is not permitted to download, forward or distribute the text or part of it, without the consent of the author(s) and/or copyright holder(s), unless the work is under an open content license such as Creative Commons.

Takedown policy
Please contact us and provide details if you believe this document breaches copyrights.
We will remove access to the work immediately and investigate your claim.

This work is downloaded from Delft University of Technology.

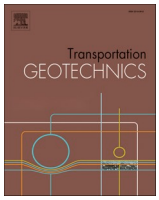
Transportation Geotechnics 59 (2026) 101965



Contents lists available at ScienceDirect

Transportation Geotechnics

journal homepage: www.elsevier.com/locate/trgeo



Modeling dynamic responses of three-dimensional high-speed train-ballasted track-subgrade coupled system subjected to spatial differential subgrade settlement

Yuanjie Xiao [a,b], Zixuan Deng [a], Sijia Zhou [c,**], Zhenxing Chang [d], Jianfeng Mao [a,*], Zehan Shen [a], Weidong Wang [a], Sui Tan [b,e]

[a] School of Civil Engineering, Central South University, Changsha 410075, China
[b] National Engineering Research Center of High-speed Railway Construction Technology, Changsha 410075, China
[c] Faculty of Civil Engineering and Geosciences, Delft University of Technology, Stevinweg 1, 2628 CN Delft, The Netherlands
[d] Department of Civil and Environmental Engineering, The Hong Kong Polytechnic University, Hung Hom, Kowloon, Hong Kong, 999077, China
[e] China Railway Group Limited, Beijing 100039, China

ARTICLE INFO

Keywords:
Train-ballasted track-subgrade coupled system
Differential subgrade settlement
Train-induced vibration
Iterative algorithm
Track irregularity

ABSTRACT

The relationship between subgrade settlement and rail deformation remains unclear, and the impact of subgrade settlement on dynamic responses of the ballasted track, as well as on the running safety and comfort of high-speed trains, has not been adequately quantified. To address such deficiency, a three-dimensional (3D) numerical model of train-ballasted track-subgrade coupled system considering spatial differential subgrade settlements was established. An innovative iterative algorithm was proposed to determine the real-time track-subgrade contact, enabling the analysis of resulting track irregularities and train-induced vibration. The results show that the number of unsupported sleepers increases with greater settlement amplitudes and shorter settlement wavelengths, while spatial differential subgrade settlement significantly affects wheel-rail interaction. Track structures located at the settlement center area on the side with less settlement, as well as those at the settlement boundary area on the side with greater settlement, are more susceptible to damage. These areas also exhibit higher dynamic vertical subgrade stress, thus aggravating differential settlement. The findings could provide theoretical basis and technical guidance for improving high-speed railway operation and maintenance practices.

Introduction

Extensive field tests and numerical simulations have demonstrated that repeated train loads induce plastic deformation in the subgrade, while the variations in subgrade soil properties, groundwater table depth, compaction quality, and other influential factors can lead to differential subgrade settlement [1–5]. Various patterns of differential subgrade settlement have been observed, including sloping, faulting, and cosine-shaped forms [6]. The differential subgrade settlement may cause long-wavelength track irregularity, accelerate track deterioration, and aggravate not only dynamic responses of railway train and track but also wheel-rail interactions [7]. As for ballasted railway track, the track superstructures are particularly susceptible to differential subgrade settlement, and the severity of differential subgrade settlement depends considerably on railway ballast and subgrade material properties [8,9]. The operational safety and ride comfort of high-speed trains are thus affected, and it becomes crucial to quantify the detrimental influences of subgrade settlement for improved operation and maintenance of ballasted track.

The common approach to evaluate the influence of differential settlement on track structures is to calculate the induced track irregularity. Cai et al. [10] developed a 3D beam-plate-solid finite element model to calculate the deformation of the double-block ballastless slab track subjected to cosine-type settlement, and analyzed the effects of

* Corresponding author.
** Co-corresponding author.
E-mail addresses: yjxiao@csu.edu.cn (Y. Xiao), dengzx@csu.edu.cn (Z. Deng), SijiaZhou_CSU@outlook.com (S. Zhou), zhxfst.chang@connect.polyu.hk (Z. Chang), jfmao1@csu.edu.cn (J. Mao), 224812187@csu.edu.cn (Z. Shen), weidong_wang0301@163.com (W. Wang), suitan2025@163.com (S. Tan).

https://doi.org/10.1016/j.trgeo.2026.101965
Received 16 October 2025; Received in revised form 18 February 2026; Accepted 23 February 2026
Available online 24 February 2026
2214-3912/© 2026 Elsevier Ltd. All rights are reserved, including those for text and data mining, AI training, and similar technologies.

settlement amplitudes and wavelengths on track irregularity and the size of gaps between track and subgrade. Chen et al. [11] proposed an analytical formula to establish the relationship between bridge pier settlement and the double-block ballastless slab track deformation for the track-bridge coupled system, and further used the obtained track deformation as the system excitation to analyze the influence of pier settlement on dynamic train performance. However, those studies primarily focused on the influence of settlement on track geometry irregularity, but neglected potential changes in track stiffness irregularity. Zhou et al. [12] derived analytical relationship between vertical deformation of continuous rail beams and that of the China Railway Track System (CRTS) I ballastless slab track, and analyzed the influences of different patterns of settlement on rail deformation. However, no further analysis on dynamic responses of the track system under train loading was performed.

The high bending stiffness of rail beams introduces significant deformation discontinuity between track superstructures and underlying subgrade, leading to voids between sleepers and ballast layers. Numerous studies have analyzed the influence of settlement-induced unsupported sleepers on structural dynamic responses of railway systems. Zou et al. [13] investigated the effect of unsupported sleepers by conducting full-scale model test of the ballasted track where the differential subgrade settlement was simulated by artificially set gaps. Zhang et al. [14] and Zhu et al. [15] used non-linear spring-dashpot models to simulate the sleeper-ballast contact and analyzed the effect of settlement-induced unsupported sleepers on wheel-rail interaction. Shi et al. [16] and Zakeri et al. [17] investigated the influence of the number of unsupported sleepers on the dynamic displacement of track structures. They indicated that unsupported sleepers tend to aggravate ballast-sleeper interactions, leading to structural damage and further threatening track stability and train operation safety. Unsupported sleepers can also contribute to additional plastic deformation of the subgrade [18]. Furthermore, the railway track transition zones are prone to differential subgrade settlement due to stiffness variations under the repeated applications of train loading, thus resulting in unsupported sleepers, increased ballast-track interaction, and accelerated degradation of track structures [19,20]. Varandas et al. [21] reported significantly increasing dynamic responses of track structures due to train passages through the transition zones, highlighting the impact of subgrade settlement on long-term in-service performance. Collectively, previous studies rely on predefined voids or simplified contact assumptions, thereby limiting their capability to capture the real-time 3D evolution of contact states and stiffness redistribution under spatially differential settlement.

Many studies have indirectly evaluated the impact of differential subgrade settlement on structural damage of track components and driving quality of trains. However, there still lacks a direct and comprehensive study on dynamic responses of the entire high-speed train-ballasted track-subgrade coupled system, specifically focusing on the effect of subgrade settlement. Previous studies established numerical models of the train-track-subgrade coupled system to evaluate the influences of different amplitude and wavelength combinations of only longitudinal differential subgrade settlement in ballasted track on the unsupported sleepers, track deterioration, and ride quality and safety [22–24]. Zhang et al. [25] studied dynamic train responses and the possibility of potential structural damage under different settlement wavelengths, amplitudes, and locations. Their results showed that the differential subgrade settlement poses a threat to the train running quality and structural safety. Sun et al. [26] proposed a two-dimensional (2D) dynamic model of the train-ballasted track coupled system and analyzed dynamic train responses caused by ballast settlement. Jiang et al. [27] established a 3D finite element model of ballastless slab track-subgrade coupled system to analyze the effects of differential subgrade settlement on dynamic responses of track structures under dynamic train loading, including track deformation, tensile stress, and interlayer contact stress. Tan et al. [28] introduced imposed uneven settlement profiles into a vehicle–track model to compute vibration responses via machine-learning techniques. The settlement was treated as a predefined geometric input, often superimposed onto track irregularities, without explicitly modeling the subgrade domain or resolving the evolving track-subgrade contact state.

In practical engineering, due to the uncertainties in the natural environment and embankment construction processes, combined with the influence of train loads, the structural properties of the subgrade are not uniformly distributed along the transverse direction. This leads to the occurrence of transverse differential settlement. As a result, uneven subgrade settlement often exhibits both longitudinal and transverse non-uniformity along the railway line. Therefore, analyzing the dynamic behavior of the train-track-subgrade coupled system under transverse differential settlement of the subgrade holds significant practical engineering value. While considerable existing studies have mainly addressed longitudinal differential subgrade settlement, lateral differential subgrade settlement is also frequently observed in engineering practices and may significantly affect track performance. Such spatially asymmetric damage patterns are difficult to capture using one-dimensional (1D) settlement assumptions, symmetric models, or static analyses, as commonly adopted in previous studies (e.g., Xu et al. [29], Xiao et al. [30], and Jiang et al. [31]). While the authors' previous study [51] established a 3D coupled framework to investigate the impact of longitudinal differential settlement, the transverse non-uniformity of subgrade deformation remains unexplored. Therefore, we extended the previous 1D settlement model into a 3D spatial settlement field, aiming to uncover the coupling effects of longitudinal and transverse gradients on vehicle safety and track stability. Fan et al. [32] analyzed the development of lateral differential subgrade settlement in permafrost regions of the Qinghai-Tibet Plateau. Based on finite element method (FEM) simulations, Cui et al. [33] evaluated the influence of lateral settlement on the deformation, interface damage, and structural damage of the ballastless slab track system. However, the dynamic responses of track structures under moving train loading were not addressed in those studies. Zhang et al. [34] established a FEM model of the train-ballastless track-subgrade coupled system to analyze the influences of the amplitude and wavelength of lateral settlement on the running safety and stability of the train. However, the relationships between differential subgrade settlement and track geometry and stiffness irregularity have not been disclosed. Li et al. [35] developed a coupled model using the hybrid finite element and multi-body dynamics (FE-MBD) method, taking into account the interlayer voiding effects within the track structure. Their study focused on the influence of transverse differential settlement of the subgrade on the deformation of ballastless track structures. However, their research was limited to ballastless tracks and did not comprehensively consider the dynamic responses of structural layers in a ballasted track system under the combined effects of longitudinal and transverse uneven settlement.

To address the aforementioned deficiencies, a refined 3D numerical model was first established for the high-speed train-ballasted track-subgrade coupled system based on a customized MATLAB® framework, considering severe spatially differential subgrade settlement in both longitudinal and lateral directions. Note that previous work mainly focused on differential subgrade settlement in the longitudinal direction only. Second, an innovative iterative method was then proposed to analyze the mapping relationship between differential subgrade settlement and track deformation, capturing real-time contact states and dynamically adjusting for track geometry and stiffness irregularities as the train moves. Finally, numerical simulation results of dynamic responses of the coupled system subjected to both spatially differential subgrade settlement and moving train loading were presented accordingly, followed by an evaluation of the running safety and ride comfort of high-speed trains. Note that such an evaluation was conducted against relevant specification limits currently enforced in China. This established numerical model features the promising potential to predict deformation-related internal subgrade problems from measured rail

surface deformation and dynamic train responses. The above-mentioned three aspects mainly consist of the novelty and contributions presented in this research work.

The contents of this paper are organized as follows. Section 2 introduces the 3D numerical model of the high-speed train-ballasted track-subgrade coupled system, including the modeling assumptions and the implementation of spatial differential subgrade settlement. Section 3 describes the validation strategy, which involves comparisons of the results obtained against both field-measured data and those from the literature. Section 4 presents a detailed analysis of the dynamic responses of the coupled system under spatial differential subgrade settlement. Finally, Section 5 summarizes and concludes the paper with key findings and engineering implications.

3D numerical model established for the coupled system

Model assumptions

To establish the 3D numerical model for the high-speed train-ballasted track-subgrade coupled system, the following assumptions were reasonably made.

(1) The high-speed train runs at a constant speed, and no sliding, climbing, or jumping interactions occur between the wheelsets and the rails.
(2) The carbody, two bogies, and four wheelsets are regarded as rigid bodies, and the primary and secondary suspensions of the train are simplified as assemblies of linear springs and dashpots.
(3) Only a representative sample of short-wave random track irregularity excitation is selected and implemented in the model so as to study the influence of differential subgrade settlement on track irregularity and dynamic responses of the coupled system.

Dynamic formulations of the coupled system

Based on the vehicle-track coupling dynamics theory [36], a 3D numerical model of the high-speed train-ballasted track-subgrade coupled system was established in this study, as shown in Fig. 1, offering a more detailed and comprehensive analysis by fully incorporating both longitudinal and lateral subgrade settlement. The multi-body dynamics (MBD) method was used to model the high-speed train, whereas the finite element method (FEM) was used to model track structures and subgrade, respectively. The ballast layer was modeled by the assemblies of discrete mass blocks, while the ballast-ballast, ballast-subgrade, and ballast-sleeper interactions were modeled by the assemblies of linear springs and dashpots.

To improve computational efficiency, the 3D vehicle model includes a single carriage with 38 degrees of freedom (DOFs), as shown in Fig. 2. For brevity, the input parameters of the vehicle model are not presented in the main body of this paper but rather listed in the Appendix I section (see Table A1). The dynamic governing equation of the vehicle system can be expressed as Eq. (1):

$$\mathbf{M_V}\ddot{\mathbf{X}}_\mathbf{V} + \mathbf{C_V}\dot{\mathbf{X}}_\mathbf{V} + \mathbf{K_V}\mathbf{X_V} = \mathbf{F_V} \tag{1}$$

where $\boldsymbol{M_V}$, $\boldsymbol{C_V}$, and $\boldsymbol{K_V}$ denote the mass matrix, damping matrix, and stiffness matrix, respectively; $\boldsymbol{F_V}$ is the force vector; and $\boldsymbol{X_V}$ is the displacement vector. Note that $\boldsymbol{X_V}$ includes the longitudinal displacements x_c, x_{ft}, and x_{bt}, lateral displacements y_c, y_{ft}, and y_{bt}, vertical displacements z_c, z_{ft}, and z_{bt}, roll displacements θ_c, θ_{ft}, and θ_{bt}, pitch displacements φ_c, φ_{ft}, and φ_{bt}, and yaw displacements Ψ_c, Ψ_{ft}, and Ψ_{bt} of the car body (denoted by the subscript "c"), front bogie (denoted by the subscript "ft"), and rear bogie (denoted by the subscript "bt"), respectively; and the longitudinal displacement x_{wi}, lateral displacement y_{wi}, vertical displacements z_{wi}, roll displacements θ_{wi}, and yaw displacement Ψ_{wi} of each wheelset (denoted by the subscript "w") (where i $= 1,2,3,4$).

The vehicle subsystem and the track subsystem are coupled by wheel-rail interaction. The normal wheel-rail contact force is calculated using the linear Hertz contact model, accounting for the contact deformation between the wheel and rail. Based on the Hertzian contact theory, the formula for calculating the normal wheel-rail contact force is provided as follows:

$$N_{ij} = [\frac{1}{G}\delta_{ij}]^{\frac{3}{2}} \tag{2}$$

where N_{ij} is the wheel-rail normal contact force; G is the wheel-rail contact constant; and δ_{ij} is the wheel-rail indentation. To simplify the calculation, the nonlinear Hertz contact can be linearized to obtain the equivalent linear wheel-rail contact stiffness:

$$K_H = \frac{dN_{ij}}{d\delta_{ij}} = 1.5G^{-\frac{3}{2}}\delta_{ij}^{\frac{1}{2}} \tag{3}$$

The tangential creep force, resulting from the relative velocity between the wheel and rail, is calculated based on Kalker's linear creep theory.

Based on the FEM theory, Euler beam elements with intermittent elastic support are used to model the rail beams, and the sleepers are regarded as rigid bodies with 6 DOFs. The rail fasteners are simulated as linear spring-dashpot elements. To account for the realistic behavior of the track system under differential subgrade settlement, the self-weights of the rails and sleepers are also considered in the numerical model to calculate the concomitant settlement and potential interfacial gaps between the track and subgrade.

Track irregularities serve as the primary excitation source for the

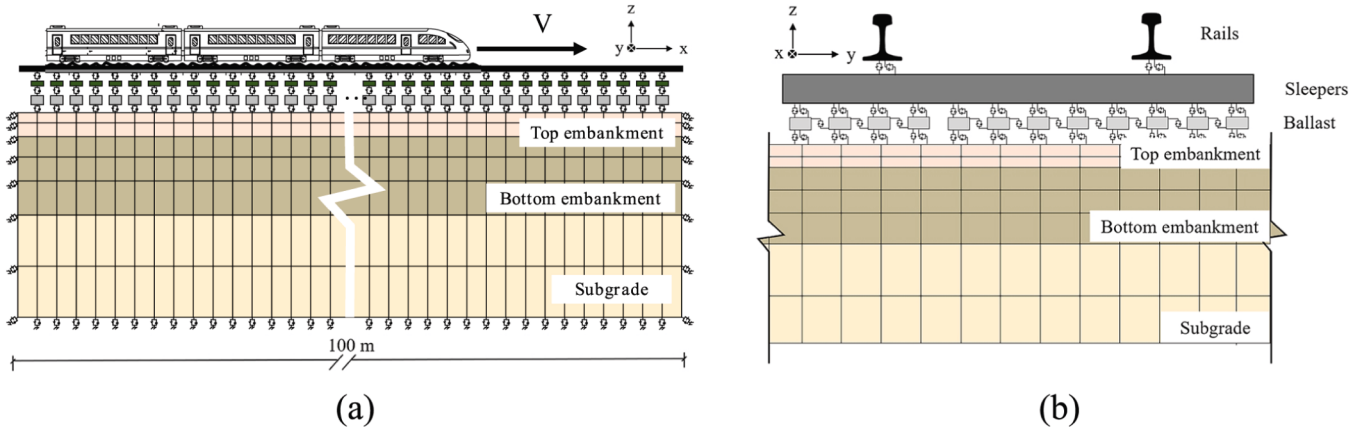


Fig. 1. Illustration of the 3D numerical model of the high-speed train-ballasted track-subgrade coupled system: (a) side view; and (b) front view.

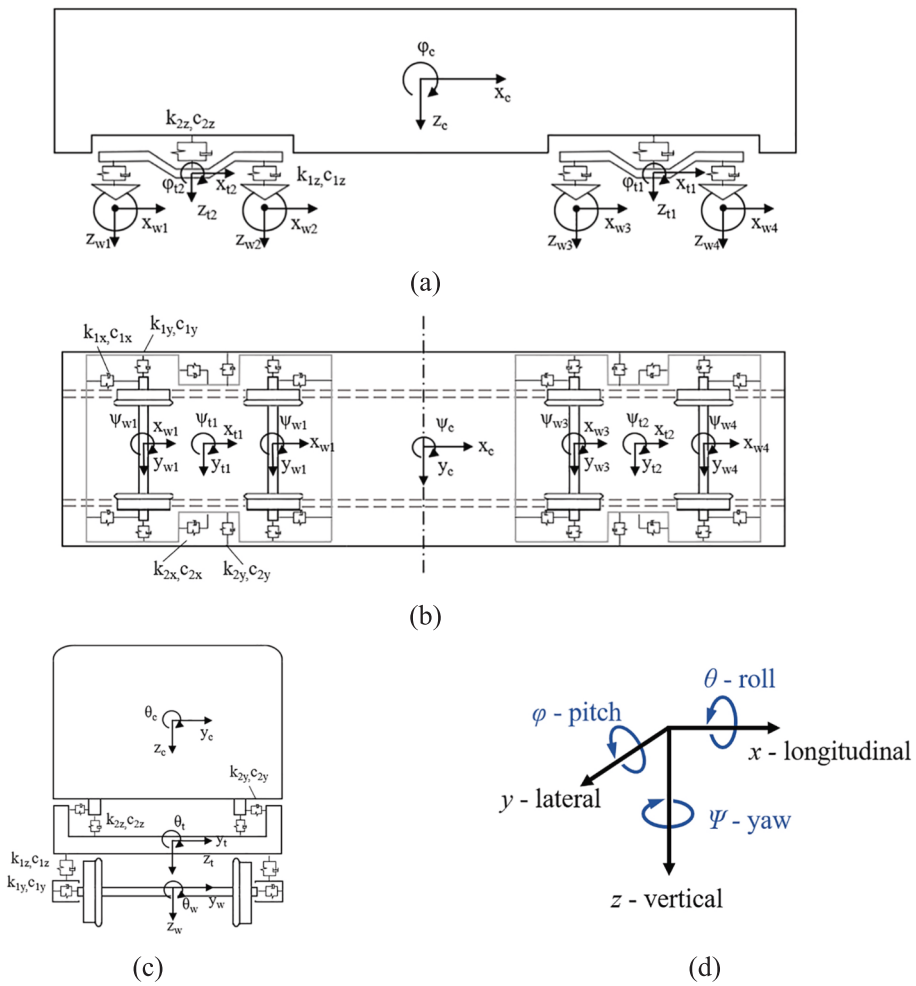


Fig. 2. Illustration of the vehicle model: (a) side view; (b) top view; (c) front view; and (d) the related coordinate system.

vehicle-track coupled system. Their influences are not limited to vibration and noise levels, but also directly affect the running comfort and operational safety of high-speed trains. In this study, the German low-interference track spectrum was adopted, comprehensively considering vertical irregularity, lateral irregularity, gauge irregularity, and alignment irregularity. These different types of irregularities were introduced into the train-track-subgrade coupled model as external excitations, thereby capturing their combined impact on the coupled system. The synthesized irregularity sequence was discretized along the rail element nodes and superimposed as initial vertical displacements of the Euler beam elements. This ensures consistency between the spatial discretization of the finite element model and the imposed irregularity excitation, thereby enabling reproducibility of the numerical simulations.

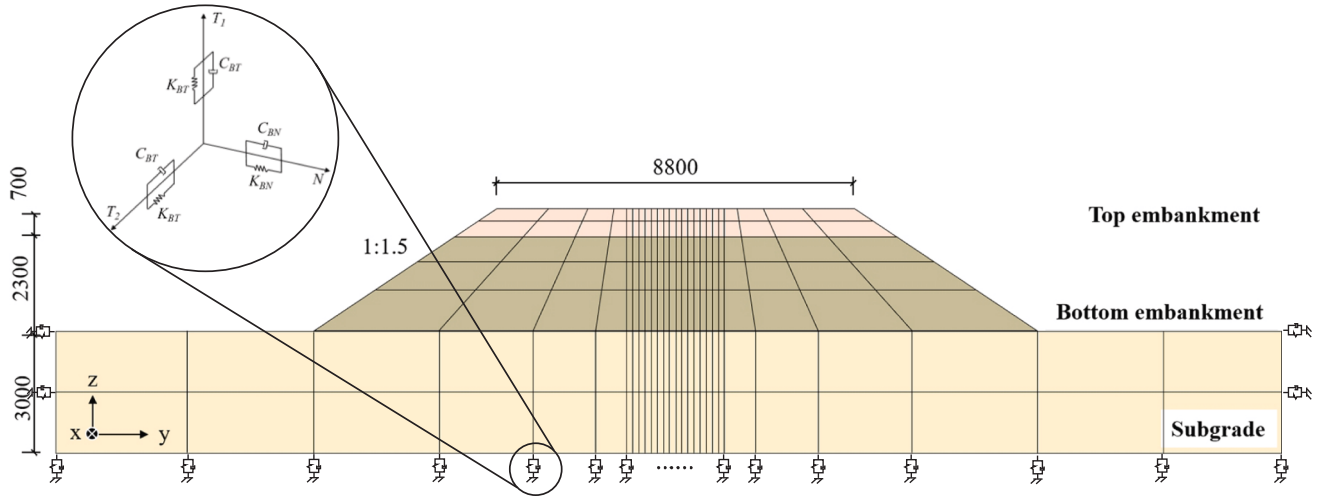


Fig. 3. Illustration of the finite element model for the subgrade of the track system (unit: mm).

Considering the discrete and particulate nature of railway ballasts, the ballast layer of the numerical model is discretized into a number of mass blocks along both longitudinal and lateral directions, in order to effectively capture the overall dynamic responses of the system while enhancing computational efficiency [37–40]. Each mass block possesses 3 DOFs in space: longitudinal displacement x , lateral displacement y, and vertical displacement z. In the numerical model, the longitudinal length of the subgrade studied is 100 m, whereas the cross-sectional size of the track system is determined according to the documentation of China's technical specification TB10621-2014 [41], as shown in Fig. 3. The subgrade consists of three different layers: the top embankment, the bottom embankment, and the natural or engineered ground. The entire subgrade is then meshed by 3D eight-node *iso*-parametric elements, and refined meshes are adopted in the regions directly below the sleepers. In this study, the track substructure was modeled using equivalent linear elastic constitutive models. To rigorously characterize the subgrade material behavior, both the linear elastic and classical Drucker-Prager (DP) elastoplastic constitutive laws were evaluated. The DP model incorporates material nonlinearity through a nonlinear incremental procedure. In this procedure, an elastic predictor-plastic corrector algorithm combined with Newton-Raphson iterations is employed to capture potential yielding and energy dissipation. However, as shown in Fig. 4, comparative simulations reveal that the transient dynamic responses (e.g., carbody and wheelset accelerations) remain highly consistent between the two models, as the dynamic stress levels during a single train passage predominantly stay within the elastic range of the compacted subgrade. While the DP model provides a detailed account of minor plastic accumulation (on the order of 10^{-4} m), it increases the computational time duration from 8 h to over 20 h per simulation due to the necessity of repetitive stiffness matrix updates and finer temporal discretization. Since the primary focus of this study is the short-term transient dynamic responses induced by spatially differential subgrade settlement, rather than long-term material degradation or settlement evolution, the linear elastic model was adopted for the extensive parametric studies. This choice ensures a high-fidelity representation of the coupling mechanisms while maintaining the computational efficiency required for a comprehensive sensitivity analysis. Representative mechanical parameters governing the dynamic stiffness of each substructure layer were selected based on design specifications, published literature, and the authors' previous validated studies, which are summarized in Appendix I (see Table A2). As shown in Fig. 3, the model applies the fixed bottom boundary and vertical roller boundaries. In addition, infinite elements were adopted in lieu of a considerable number of far-field elements with accuracy unaffected, thus creating "silent" boundaries for the coupled dynamic analysis.

In the development of the finite element model for analyzing dynamic responses of the track-subgrade coupled system, the analysis can only be conducted on a subgrade of limited length and depth due to computational limitations. Considering the reflection and superposition of stress waves at the model boundaries, as well as the semi-infinite nature of the subgrade, it is essential to reasonably define the model boundaries to ensure the accuracy of the simulation results. In this study, the commonly used 3D viscoelastic artificial boundary was applied to the subgrade to impose boundary conditions for dynamic analysis. Liu et al. [42] provided a detailed explanation of this boundary condition. The fundamental concept involves placing spring-damper elements, or equivalent spring-damper elements, along the artificial boundaries to simulate an infinite subgrade. By applying a 3D viscoelastic artificial boundary to the ballasted track-subgrade coupled dynamic finite element model, wave reflections at the model boundaries are reduced, thereby improving the accuracy of the simulation results. Since the parameters of the spring-damper elements at boundary nodes vary with the loading position, a simplification was adopted in this study, where identical spring-damper parameters were assigned to all boundary nodes around the subgrade.

Modelling differential subgrade settlement

The relationship between subgrade settlement and ballast layer settlement is extremely complicated. Previous studies assumed that the deformation of the discrete ballast layer is consistent with that of the top embankment, which can effectively reduce calculation time but still ensure the necessary accuracy of calculation results [23,26]. In this study, the same assumption was also adopted to reasonably simplify the numerical model. Using standardized or idealized settlement patterns can better reveal the general patterns and effects of different settlement modes and amplitudes on the overall structural responses of the track. Field monitoring has shown that subgrade settlement profiles often exhibit smooth, continuous wave-like shapes. In particular, for long-wavelength settlements, the distribution characteristics closely match those of a cosine function [43–45]. The cosine-type one, as formulated in Eq. (4), is most commonly used in high-speed railway subgrade settlement simulation and thus was selected for this numerical model.

$$Z(x) = \frac{h}{2}\left(1 - \cos\left(\frac{2\pi x}{L}\right)\right) \tag{4}$$

where Z denotes the subgrade settlement along the driving (longitudinal) direction; x is the coordinate of each point along the driving direction; L is the wavelength of the cosine-type differential subgrade settlement; and h is the settlement amplitude, which is assumed to be uniform in the lateral direction.

In actual railway tracks, it is common to observe both lateral and longitudinal differential subgrade settlement, as illustrated in Fig. 5. Accurately representing these settlements in numerical simulations is

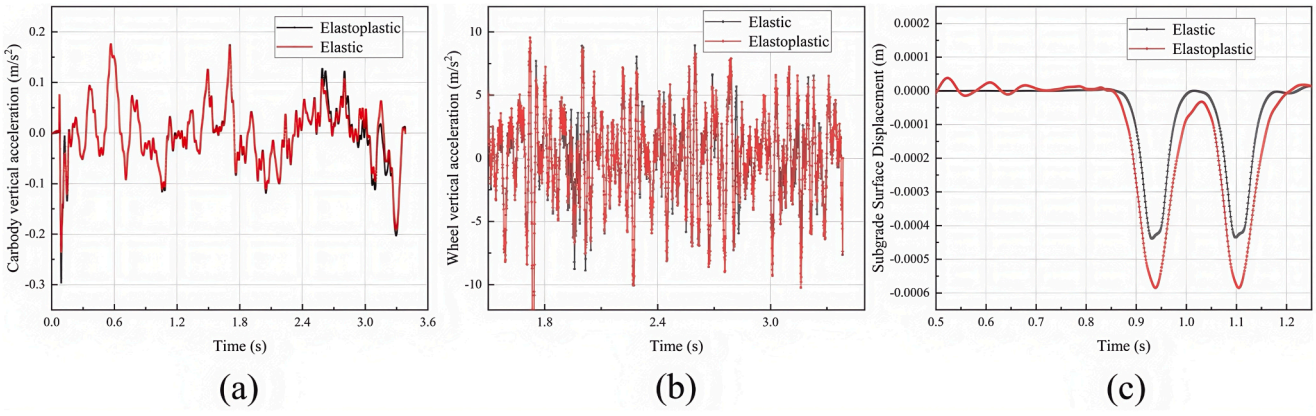


Fig. 4. Comparison of dynamic responses between the linear elastic and classical Drucker-Prager (DP) elastoplastic models for the subgrade: (a) vertical acceleration of the carbody; (b) vertical acceleration of the wheelset; and (c) surface displacement of the subgrade.

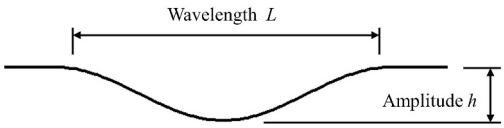


Fig. 5. Illustration of the cosine-type differential subgrade settlement.

essential to comprehensively investigate the impact of severe spatial differential subgrade settlement on dynamic responses of the coupled system. Therefore, the numerical model established in this study incorporated settlements in both directions, which have varying amplitudes but identical wavelength, as formulated in Eq. (5).

$$Z(x,y) = \left(\frac{(y - y_L) \times \Delta h}{2W} + \frac{h_L}{2}\right)\left(1 - \cos\left(\frac{2\pi x}{L}\right)\right) \quad (5)$$

where Z denotes the subgrade settlement at each point; x is the coordinate of each point along the driving direction; y is the coordinate of each point along the lateral direction; y_L is the y-coordinate of the left rail; Δh is the difference of the subgrade settlement between under the left and the right rails (see Fig. 6); W is the track gauge (see Fig. 6); and L is the wavelength of cosine-type differential subgrade settlement.

The different scenarios of subgrade settlement simulated in this study are detailed in Table 1. To systematically assess the effects of varying lateral settlement amplitudes, the lateral amplitude differences are set to range from 5 mm to 30 mm, labeled as Case 1 through Case 6, each with a constant wavelength of 20 m. Conversely, to investigate the influence of different wavelengths on the structural responses, the wavelengths are set to vary from 10 m to 35 m, denoted as Case 7 through Case 12, while maintaining a fixed lateral amplitude difference of 20 mm. Although design standards specify the maximum allowable settlement amplitude, subgrade settlement may exceed these limits under certain extreme conditions, such as natural disasters, construction accidents, or other unforeseen events. Since both natural and human factors can cause asymmetric settlement on either side of the track, transverse settlement differences ranging from 5 mm to 30 mm are considered. This range enables the simulation of conditions from minor to severe settlement, allowing for the assessment of their impact on track performance. The settlement wavelength varies from 10 m to 35 m, covering a spectrum from short to long wavelengths, which facilitates the investigation of the influence of wavelength on structural responses [46]. This scheme enables a comprehensive investigation of the coupled system's behavior under extreme conditions and facilitates the assessment of existing design margins. It ensures that the system remains safe and stable, even when actual conditions exceed anticipated levels. By simulating this extreme case, it is possible to ensure that the model can provide reliable results under a variety of conditions.

Mapping relations between differential subgrade settlement and track irregularity

It can be observed from Fig. 7 that the self-weights of the rails and sleepers can induce concomitant settlement upon the occurrence of differential subgrade settlement, thus contributing to the track geometry irregularity. Further, the high bending stiffness of rails may cause unsupported sleepers and upwarping deflection of the rails, leading to

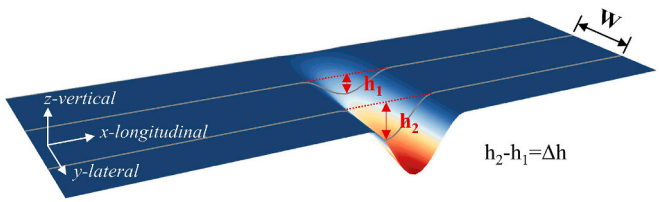


Fig. 6. Illustration of lateral differential subgrade settlement.

Table 1
Different wavelength and amplitude combinations of differential subgrade settlement simulated.

Case No.	Wavelength (m)	Amplitude under left rail (mm)	Amplitude under right rail (mm)	Amplitude difference Δh (mm)
1	20	10	15	5
2	20	10	20	10
3	20	10	25	15
4	20	10	30	20
5	20	10	35	25
6	20	10	40	30
7	10	10	30	20
8	15	10	30	20
9	20	10	30	20
10	25	10	30	20
11	30	10	30	20
12	35	10	30	20

Table 2
Limiting values of structural dynamic responses of high-speed rail.

Parameter	Value
Vertical carbody acceleration (g)	0.13
Lateral carbody acceleration (g)	0.10
Vertical wheel-rail contact force (kN)	170
Lateral wheel-rail contact force (kN)	$0.85(15 + P_w/3)$
Wheel unloading rate	0.6

Note: P_w denotes the static axle load.

greater contact forces on adjacent sleepers. The repeated moving train loading also induces repeated impacts between the track and underlying subgrade. Therefore, the relationship between differential subgrade settlement and track irregularity needs to be studied first.

In this study, a 3D MBD-FEM model of the high-speed train-ballasted track-subgrade coupled system subjected to spatially differential subgrade settlement was established by MATLAB® program. An iterative algorithm was proposed to calculate the relationship between subgrade settlement and track irregularity under the combined applications of moving train loading and self-weights. The iterative calculation steps are illustrated in Fig. 8. The iterative algorithm starts at time zero, initially assuming full contact between the sleepers and ballast. The process then enters the iteration loop. First, the contact state between the sleepers and ballast is calculated using the relevant formulas, and the contact condition is determined based on their vertical displacements while simultaneously updating the contact matrix for the current time step. If the contact state is the same as that in the previous step, the forces on the sleepers and ballast are computed according to the formulas. The time step is then incremented, and the structural dynamic responses and deformation under the train load are calculated using the Wilson-θ integration method, with the contact matrix updated accordingly. If the contact state converges again at this point, the results for the current time step are recorded. The algorithm then checks whether the train is still within the calculation region. If it has not yet exited, the iteration proceeds to the next time step. If the train has left the region, the algorithm terminates. Throughout the process, the continuous updating of the contact state and dynamic responses enables the iterative calculation of structural responses as the train passes through the track section. The impacts of the settlement on dynamic responses of the track-subgrade coupled system and running safety and ride comfort of the high-speed train are evaluated accordingly.

To formulate the sleeper-ballast contacts in the numerical model, the contact state matrix $\boldsymbol{S_n}$ shown in Eq. (6) is introduced. It is assumed that no tensile contact forces are allowed between sleepers and ballasts upon the occurrence of upwarping rails or unsupported sleepers, i.e., the contact forces between sleepers and ballasts are zero under such circumstances. It is worth noting that the Heaviside function in this study

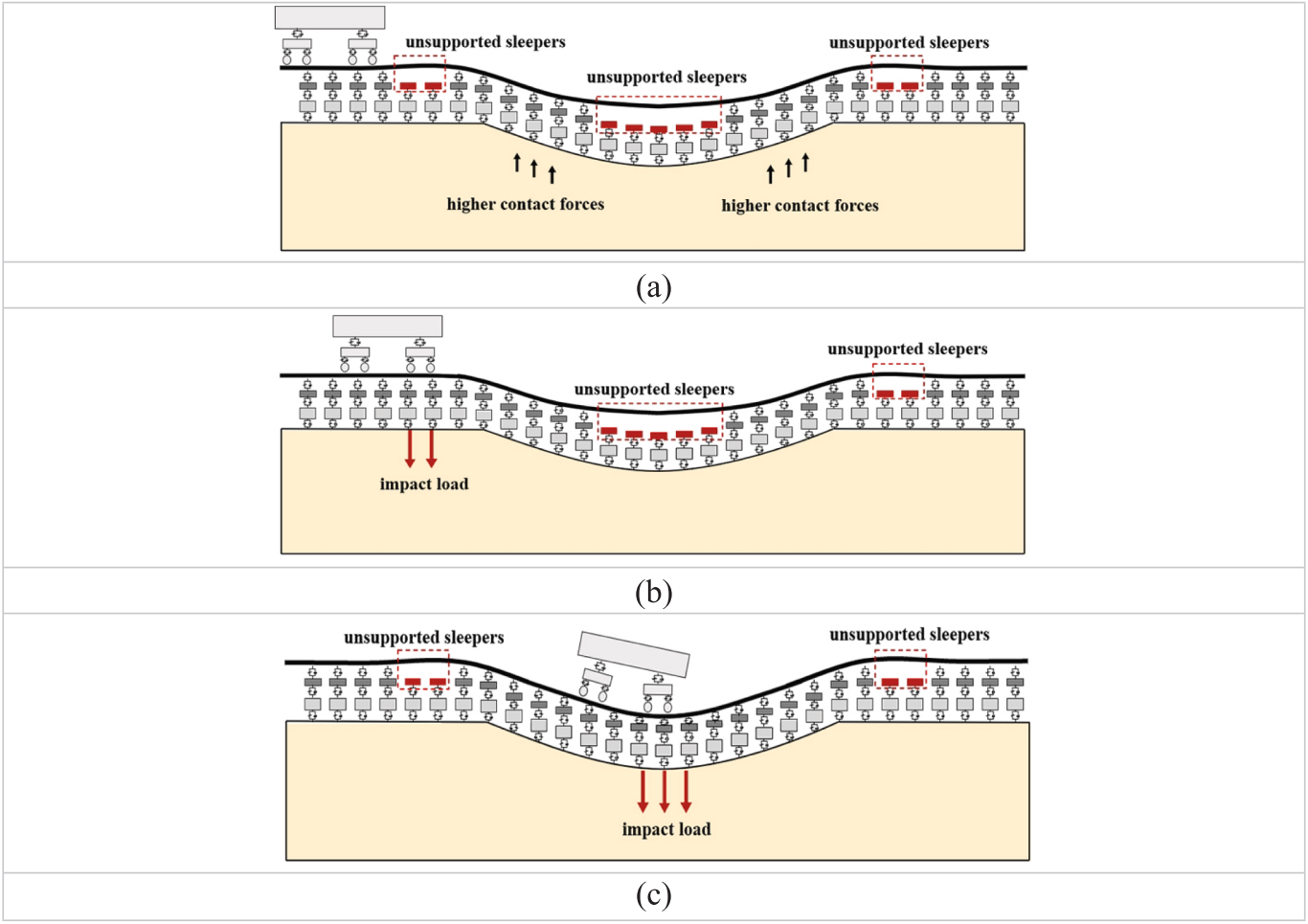


Fig. 7. Schematic diagrams of interface contact variations during the passage of moving train due to differential subgrade settlement: (a) the train is in non-settlement area; (b) the train is in the edge of settlement area; and (c) the train is in the center of settlement area.

was used to represent the binary contact or separation between sleepers and ballast, aiming to capture the macroscopic phenomenon of sleeper voids under spatially differential settlement and its effect on the overall dynamic responses of the 3D train-track-subgrade coupled system, rather than modeling microscale ballast particle compaction and re-support. The focus was on dynamic amplification, wheel-rail interaction, and structural load redistribution during single or few train passages, where abrupt stiffness changes caused by sleeper voids dominate transient responses. The idealized contact-separation model has been widely applied in ballasted track dynamics and effectively captures macroscopic response characteristics without significantly affecting qualitative trends. Although neglecting local re-support may slightly overestimate dynamic impacts in this study, this conservative assumption is acceptable for evaluating operational safety and wheel-rail forces and for identifying potential damage zones. Future studies could be conducted to combine DEM with the macroscopic dynamic framework to perform multi-scale coupled analysis of ballast compaction and re-support, which is currently underway.

$$\boldsymbol{S}_n = \begin{bmatrix} s_{11} & s_{12} & \cdots & s_{1j} \\ s_{21} & s_{22} & \cdots & s_{2j} \\ \vdots & \vdots & \ddots & \vdots \\ s_{i1} & s_{i2} & \cdots & s_{ij} \end{bmatrix} \tag{6}$$

where $s_{ij} = \delta(z_{sl}^{(ij)} - z_b^{(ij)})$; $\delta(\cdot)$ is the Heaviside function with values of 0 and 1 indicating the loss and existence of sleeper-ballast contacts, respectively; $z_b^{(ij)}$ is the vertical displacement of the ballast layer; and $z_{sl}^{(ij)}$ is the vertical displacement of each point on individual sleepers, which can be calculated from the vertical displacement of the sleeper center and the angle about the X-axis via $z_{sl}^{(ij)} = z_{sl}^{(i)} + \theta^{(i)} l^{(j)}$.

At static equilibrium, the dynamic formula of the track-subgrade system is expressed as Eq. (7):

$$\begin{bmatrix} \boldsymbol{K}_r & \boldsymbol{K}_{rt} & & \\ \boldsymbol{K}_{tr} & \boldsymbol{K}_t & & \\ & & \boldsymbol{K}_b & \boldsymbol{K}_{bs} \\ & & \boldsymbol{K}_{sb} & \boldsymbol{K}_s \end{bmatrix} \begin{Bmatrix} \boldsymbol{X}_r \\ \boldsymbol{X}_t \\ \boldsymbol{X}_b \\ \boldsymbol{X}_s \end{Bmatrix} = \begin{Bmatrix} \boldsymbol{m}_r \boldsymbol{g} \\ \boldsymbol{m}_t \boldsymbol{g} - \boldsymbol{K}_{tb}^n \boldsymbol{X}_t \\ \boldsymbol{F}_b^* - \boldsymbol{K}_{bt}^n \boldsymbol{X}_b \\ \boldsymbol{F}_s^* \end{Bmatrix} \tag{7}$$

where K_r, K_t, K_b, and K_s represent the stiffness matrices of the rail, sleeper, ballast, and subgrade, respectively; K_{rt}, K_{tb}, and K_{bs} denote the contact stiffness matrices between the rail and sleeper, sleeper and ballast, and ballast and subgrade, respectively; X_r, X_t, X_b, and X_s are the displacement vectors of the rail, sleeper, ballast, and subgrade, respectively; and $m_r g$ and $m_t g$ represent the self-weights of the rail and sleeper, respectively, while F_b and F_s are the equivalent forces corresponding to the uneven settlement of the ballast bed and subgrade.

The dynamic formula of the high-speed train-ballasted track-subgrade coupled system under moving train loading is expressed by Eq. (8):

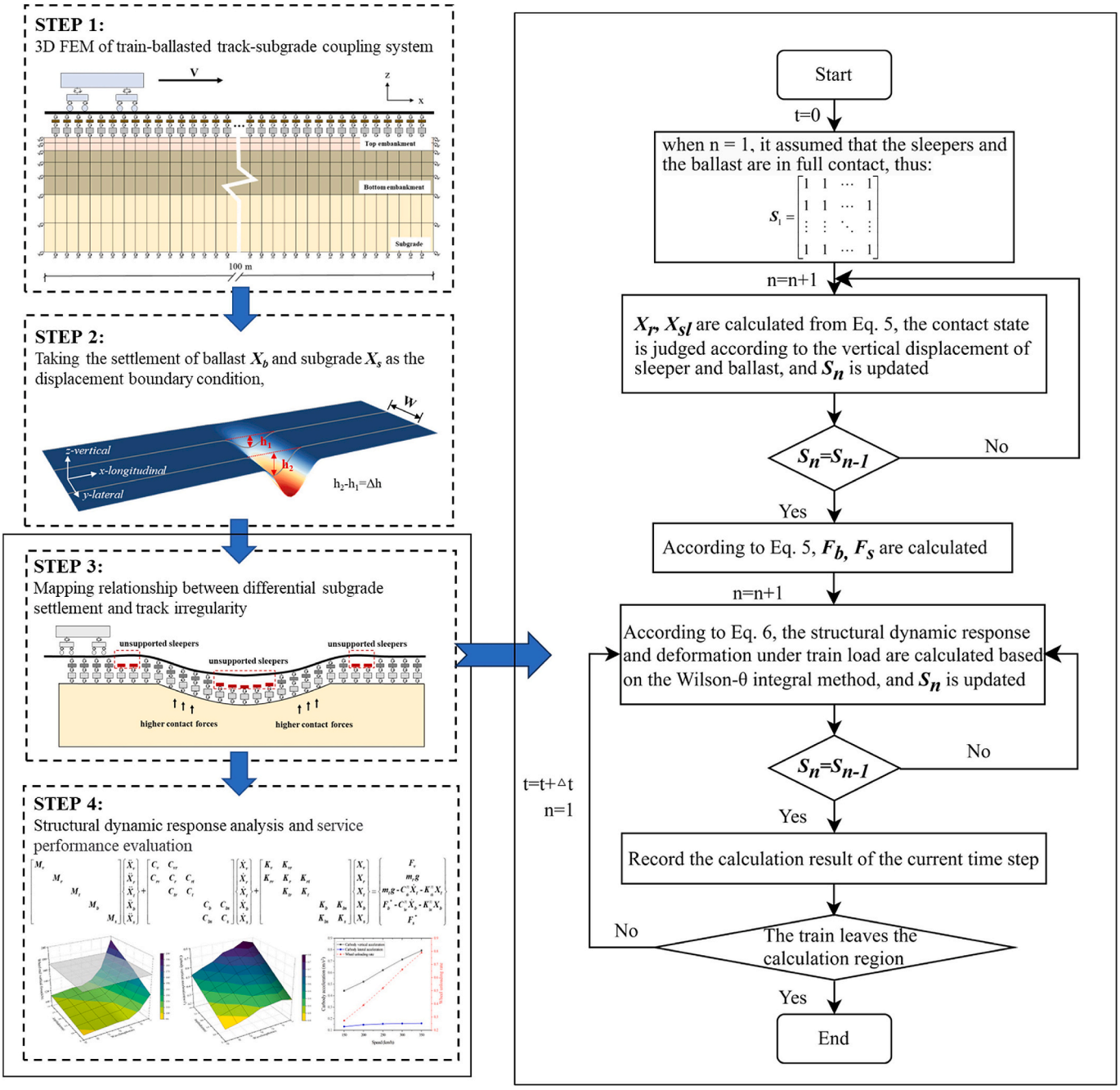


Fig. 8. Schematic diagram of the calculation flowcharts of the iterative algorithm.

$$\begin{bmatrix} M_v & & & & & \\ & M_r & & & & \\ & & M_t & & & \\ & & & M_b & & \\ & & & & M_s \end{bmatrix} \begin{Bmatrix} \ddot{X}_v \\ \ddot{X}_r \\ \ddot{X}_t \\ \ddot{X}_b \\ \ddot{X}_s \end{Bmatrix} + \begin{bmatrix} C_v & C_{vr} & & & \\ C_{rv} & C_r & C_{rt} & & \\ & C_{tr} & C_t & & \\ & & & C_b & C_{bs} \\ & & & C_{bs} & C_s \end{bmatrix} \begin{Bmatrix} \dot{X}_v \\ \dot{X}_r \\ \dot{X}_t \\ \dot{X}_b \\ \dot{X}_s \end{Bmatrix}$$

$$+ \begin{bmatrix} K_v & K_{vr} & & & \\ K_{rv} & K_r & K_{rt} & & \\ & K_{tr} & K_t & & \\ & & & K_b & K_{bs} \\ & & & K_{bs} & K_s \end{bmatrix} \begin{Bmatrix} X_v \\ X_r \\ X_t \\ X_b \\ X_s \end{Bmatrix} = \begin{Bmatrix} F_v \\ m_r g \\ m_t g - C_{tb}^n \dot{X}_t - K_{tb}^n X_t \\ F_b^* - C_{bt}^n \dot{X}_b - K_{bt}^n X_b \\ F_s^* \end{Bmatrix} \tag{8}$$

where $K_{bt}^n = K_{tb}^{nT}$ is the equivalent stiffness matrix of sleepers or ballasts for full sleeper-ballast contact, and $K_{tb}^n = S_n \otimes K_{tb} = \begin{bmatrix} s_{11}k_{11} & s_{12}k_{12} & \cdots & s_{1i}k_{1i} \\ s_{21}k_{21} & s_{22}k_{22} & \cdots & s_{2i}k_{2i} \\ \vdots & \vdots & \ddots & \vdots \\ s_{i1}k_{i1} & s_{i2}k_{i2} & \cdots & s_{ii}k_{ii} \end{bmatrix}$; and $C_{bt}^n = C_{tb}^{nT}$ is the equivalent damping matrix of sleepers or ballasts for full sleeper-ballast contact, and $C_{tb}^n = S_n \otimes C_{tb} = \begin{bmatrix} s_{11}c_{11} & s_{12}c_{12} & \cdots & s_{1i}c_{1i} \\ s_{21}c_{21} & s_{22}c_{22} & \cdots & s_{2i}c_{2i} \\ \vdots & \vdots & \ddots & \vdots \\ s_{i1}c_{i1} & s_{i2}c_{i2} & \cdots & s_{ii}c_{ii} \end{bmatrix}$.

Regarding the convergence and computational efficiency of the iterative algorithm, the convergence during each iteration is judged by comparing the track-ballast contact state matrix S_n with that from the previous iteration S_{n-1}, i.e., the iteration terminates when $S_n = S_{n-1}$,

ensuring that the contact state accurately reflects the actual stress conditions under uneven subgrade settlement and train loading. For cosine-type uneven subgrade settlements with different wavelengths and amplitudes, the iterative method converges within a limited number (typically 3 ~ 10) of iterations. Simulations under various settlement combinations demonstrate that the algorithm is reliable and can stably compute the accompanying deformations of the track structures. This iterative method combines static equilibrium solving with contact state updates, updates the contact state only within each time step, and avoids repeated assembly of global stiffness matrix, thereby significantly improving computational efficiency without introducing additional degrees of freedom. To further illustrate the physical manifestation of this iterative process, Fig. 9 presents the evolution of the sleeper-ballast gap during wheel passage. The results demonstrate that the algorithm accurately captures the non-linear transition from an initial gap to a fully closed contact state, which remains numerically stable even under extreme settlement amplitudes (up to 35 mm). This precise identification of interfacial status changes ensures that the local stiffness updates are consistent with the structural deformation, thereby providing a robust physical basis for the observed rapid convergence and computational stability in large-scale 3D simulations. Compared with the discrete element method (DEM), it offers a notable computational advantage. For 3D models of track segments with dimensions in the order of hundreds of meters, the computation time is acceptable, making the method suitable for large-scale 3D coupled dynamic analyses. Moreover, the method can effectively predict sleeper void positions, wheel-rail load distributions, and track geometry irregularities, thus offering broad engineering applicability while balancing accuracy and efficiency. Therefore, the iterative method proposed and employed in this study ensures convergence and computational stability while maintaining high efficiency, satisfying the requirements for dynamic analysis of large-scale 3D track-subgrade coupled systems.

Numerical model validation

The numerical model established in this study for the coupled system was further validated by comparing the simulation results against field-measured data from a high-speed railway reported by Luo et al. [47]. The field monitoring was conducted on a double-track ballasted railway section of the Beijing-Zhangjiakou high-speed railway line in China, where the dynamic responses of the track-subgrade system under train loading were recorded. The test train was the CRH380AJ comprehensive inspection train with a 6M + 2T configuration (eight vehicles in total), operating at speeds up to 295 km/h. The monitored responses mainly included the vertical dynamic stress and vibrational responses at the subgrade surface beneath the rail-sleeper interaction zone.

In the numerical simulations, the train configuration and operating conditions were defined to be consistent with those reported elsewhere in the literature [47], ensuring comparability between the numerical results and the field measurements. In addition, the simulated random track irregularities were generated based on the classic German track spectrum. For brevity, detailed descriptions of the train configuration and simulation parameters, aforementioned in Section 2.2, are not reiterated herein. Fig. 10 shows the comparisons of field-measured and corresponding model-simulated results of dynamic responses of the top embankment. It can be observed that reasonably satisfactory agreement is achieved between field measurements and numerical simulation results, confirming the validity and accuracy of this model.

To further validate the proposed iterative algorithm for calculating the concomitant deformation of track structures, the vertical deformation responses of the rails and sleepers caused by differential subgrade settlement with a wavelength of 10 m and an amplitude of 15 mm were calculated accordingly. Fig. 11 compares the results calculated by the iterative algorithm proposed in this study and by a semi-analytical method in the literature [26]. Note that Z_r, Z_{sl}, and Z_b denote the vertical deformation of the rail, sleeper, and ballast, respectively. It can be observed from Fig. 11 that slight deviations exist between the calculation results by both methods probably due to the difference in sleeper spacing between the numerical model used herein and that in the literature. In general, the results are consistent and match well. Therefore, the rationality and accuracy of the proposed iterative algorithm and related computational framework for calculating the concomitant deformation of the track structures are verified. As compared to the analytical solutions, the MBD-FEM simulations are much more accurate and versatile in analyzing 3D dynamic responses.

Results and analysis

Effect of differential subgrade settlement on track irregularity

Fig. 12 presents a comparison between the deformation at various points along the left and right rails and the subgrade settlement directly

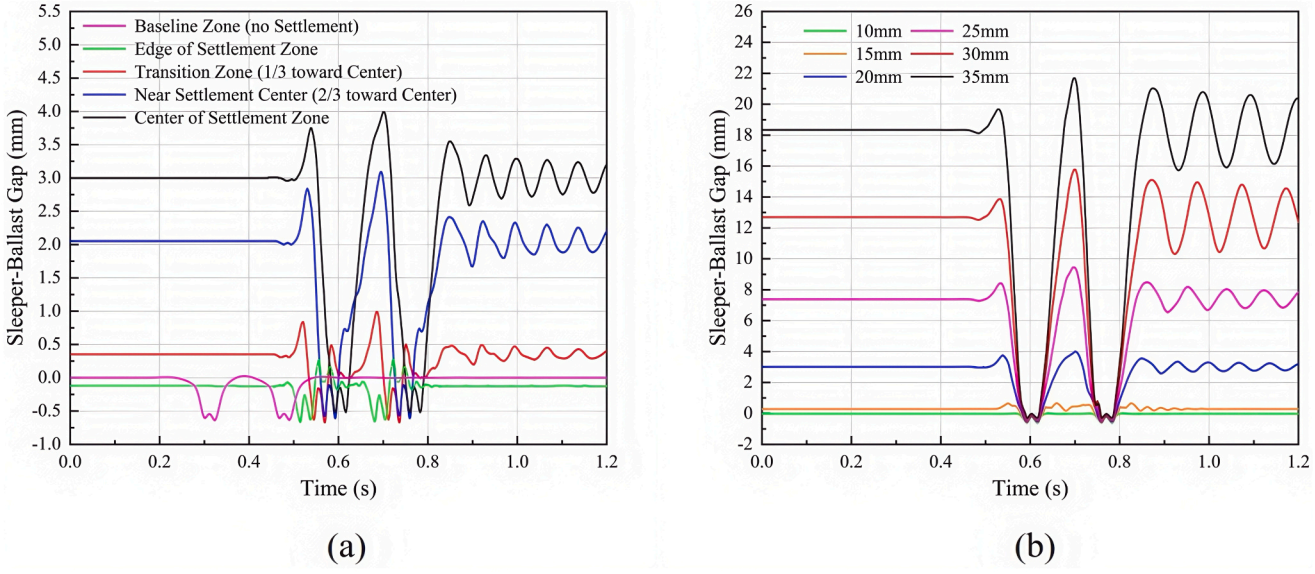


Fig. 9. Spatial evolution and sensitivity validation of the sleeper-ballast gap history: (a) spatial evolution across the settlement zone from edge to center (h = 20 mm); and (b) influence of varying settlement amplitudes (h = 10 mm to 35 mm) at the settlement center.

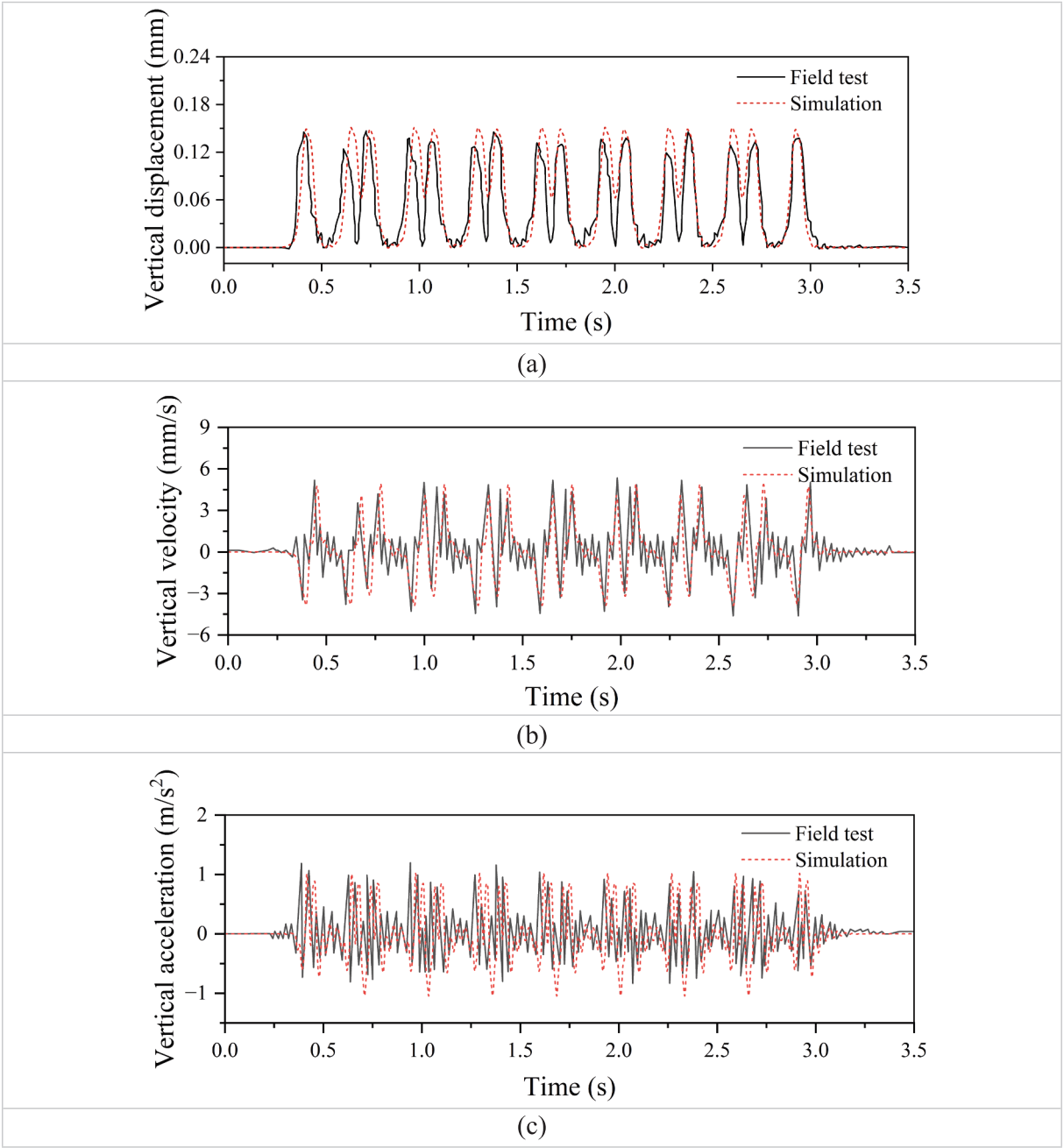


Fig. 10. Comparisons of field-measured and model-calculated dynamic responses of the top embankment layer of the coupled system: (a) vertical displacement; (b) vertical velocity; and (c) vertical acceleration.

beneath the rails. Fig. 12 plots the vertical displacement of each component in the track-subgrade system, with a fixed wavelength of 20 m and a lateral settlement amplitude of 20 mm (refer to Case 4 in Table 1). The displacement profiles clearly depict the influence of the high bending stiffness of rails on their response to underlying subgrade settlements. On the left side (i.e., the side with less settlement), the rail exhibits an upward arching near the settlement boundary areas, with a maximum upwarping displacement of 0.64 mm. Additionally, the maximum vertical displacement at the settlement center is −7.50 mm. Conversely, on the right side (i.e., the side with greater settlement), the rail shows no upwarping displacement, but a significant vertical downward displacement of −17.31 mm at the settlement center area. Since the rail deformation is less than the subgrade settlement, the track separates from the subgrade, resulting in “unsupported sleepers”. These observations indicate that differential subgrade settlement has a significant impact on the contact state between the track and subgrade.

It is worth noting that the vertical displacement responses of each individual track layer, as shown in Fig. 12, are directly obtained from the 3D train-ballasted track-subgrade coupled model in this study. Specifically, rail and sleeper displacements are solved via the finite element method, considering wheel-rail interaction, fastener forces, and ballast support, with the track-subgrade contact state updated iteratively in real time. Ballast and subgrade displacements are obtained from nodal responses under external loads and self-weights. All displacements are output in a unified coordinate system, ensuring comparability across different layers. The greater vertical displacement of the subgrade shown in Fig. 12, as compared to those of rails and sleepers, arises from differences in stiffness and load transfer. Rails and sleepers are high-stiffness components of which vertical deformation is constrained by bending rigidity and fasteners, effectively distributing

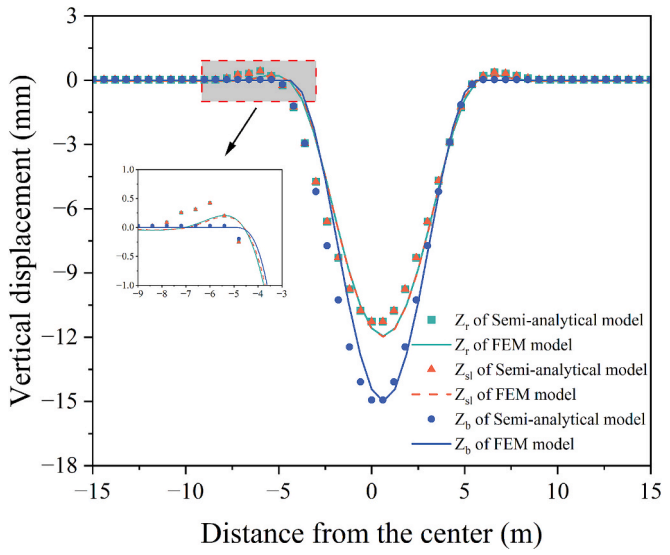


Fig. 11. The comparisons of the concomitant deformation results of track structures calculated by the iterative method proposed in this study and by the semi-analytical method in the literature.

wheel-rail loads. In contrast, the subgrade is typically a lower-stiffness continuous soil layer that bears concentrated and repeated dynamic loads, leading to larger vertical deformation. Additionally, spatially differential settlement can cause local track-subgrade separation, producing "cantilever" or "bridging" effects that limit track layer deformation and further concentrate loads onto the subgrade. These mechanisms actually explain the observed differences in vertical displacements among such different track structural layers.

To elucidate the impact of differential subgrade settlement on track deformation, the vertical deformations of both rails were calculated under various combinations of settlement wavelength and amplitude. Fig. 13 presents the rail deformation results corresponding to the subgrade settlement wavelength of 20 m and the lateral settlement amplitude ranging from 5 mm to 30 mm. From Fig. 13, it is evident that, at a constant wavelength, the difference in deformation between the two rails gradually expands and tends to stabilize as the lateral settlement amplitude increases. The left rail exhibits a decreasing vertical displacement trend, indicating that the gap between the left rail and subgrade increases with increasing lateral settlement amplitude. This occurs because the displacement of the left rail is influenced by the condition of the right rail. As the right rail undergoes pronounced downward settlement, it imposes a relative tension or levering effect on the left rail through the sleepers, causing the left rail to bend upward relative to the right rail and reducing the magnitude of its vertical displacement. Meanwhile, the range of the deformation curve for the right rail broadens accordingly.

Fig. 14 illustrates the vertical rail deformation curves for a constant lateral settlement amplitude of 20 mm, with the settlement wavelength ranging from 10 m to 35 m. At a constant amplitude level, an increase in settlement wavelength leads to corresponding increases in both the wavelengths and amplitudes of the rail deformation curves. This suggests a reduction in the gaps between the track and the subgrade, although the deformation difference between the two rails continues to grow.

Fig. 15 summarizes the maximum gap between rails and subgrade at the settlement center area under various combinations of settlement wavelength and amplitude. It indicates that the gap values on both sides progressively increase with decreasing wavelength and increasing amplitude of subgrade settlement, respectively. In addition, lower wavelengths and higher amplitudes can result in more significant loss of contact between rails and subgrade.

Effect of differential subgrade settlement on train dynamic responses

Fig. 16 shows the vertical and lateral wheel-rail contact forces for different lateral amplitude levels (ranging from 5 mm to 30 mm) with a constant 20-m settlement wavelength (Case 1 to Case 6 in Table 1). Overall, the time-history curves of vertical wheel-rail contact force exhibit a decreasing trend when the wheelset enters the settlement area, followed by an increasing trend as the wheelset passes through the center of settlement area and then a decreasing trend again upon exiting. Fig. 16(a) clearly demonstrates that the vertical wheel-rail contact force increases with increasing lateral settlement amplitude, and the difference in vertical wheel-rail contact force between the left and right rails also expands accordingly. The vertical wheel-rail contact force on the left rail experiences a slight increase from 100.09 kN to 108.35 kN. In contrast, the force on the right rail increases more significantly from 101.50 kN to 112.03 kN, representing an increase of nearly 10.34%. On the other hand, Fig. 16(b) reveals that the lateral wheel-rail contact

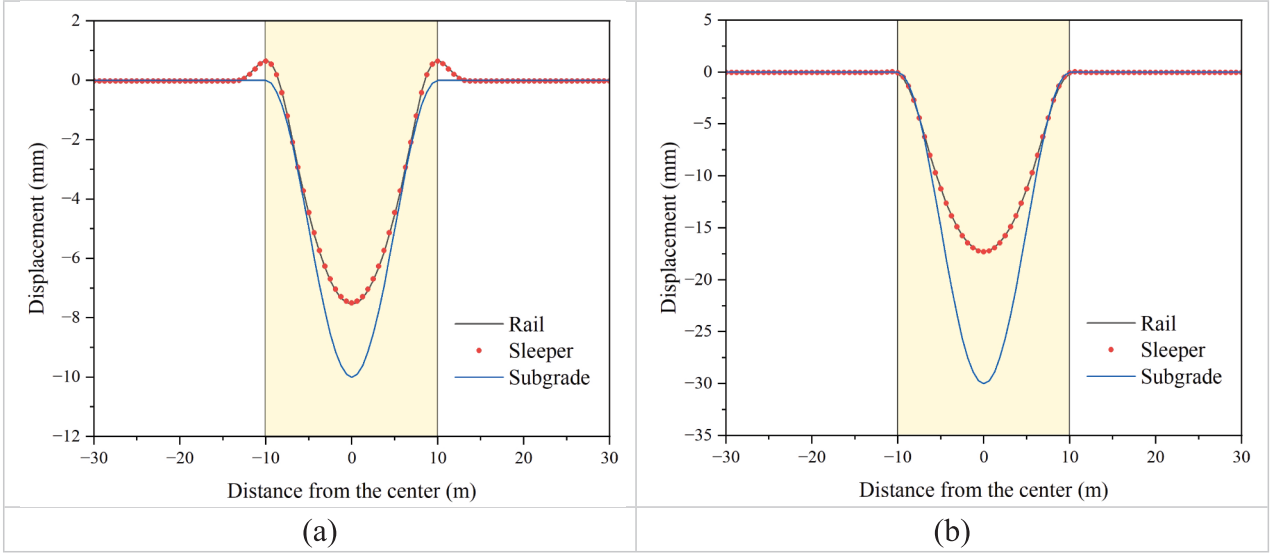


Fig. 12. The model-calculated vertical displacement responses of individual components of the track-subgrade coupled system subjected to differential subgrade settlement at (a) the left rail and (b) the right rail sides.

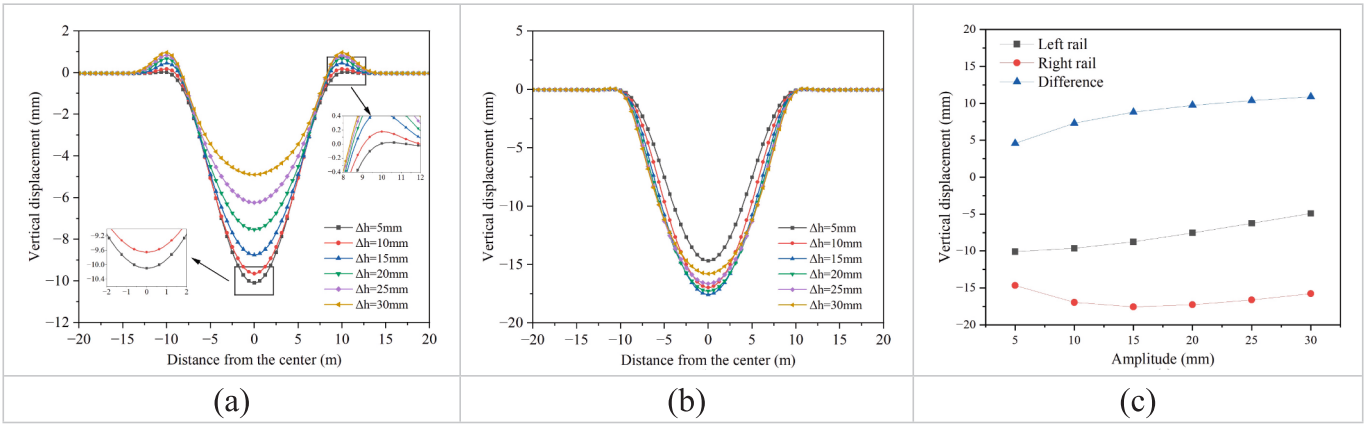


Fig. 13. Vertical rail displacement under different amplitude levels of differential subgrade settlement: (a) the left rail; (b) the right rail; and (c) the displacement difference between the left rail and the right rail.

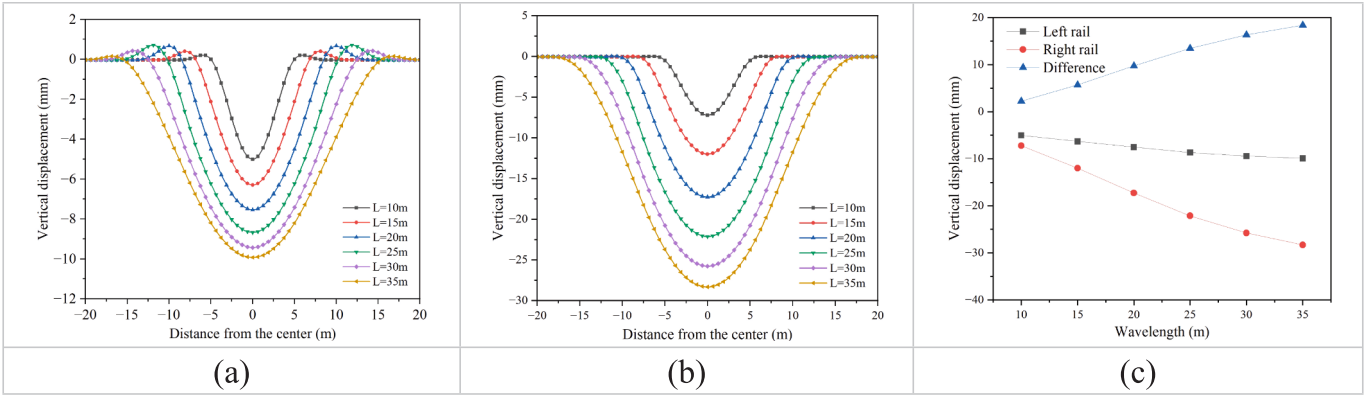


Fig. 14. Vertical rail displacement under different wavelength levels of differential subgrade settlement: (a) the left rail; (b) the right rail; and (c) the displacement difference between the left rail and the right rail.

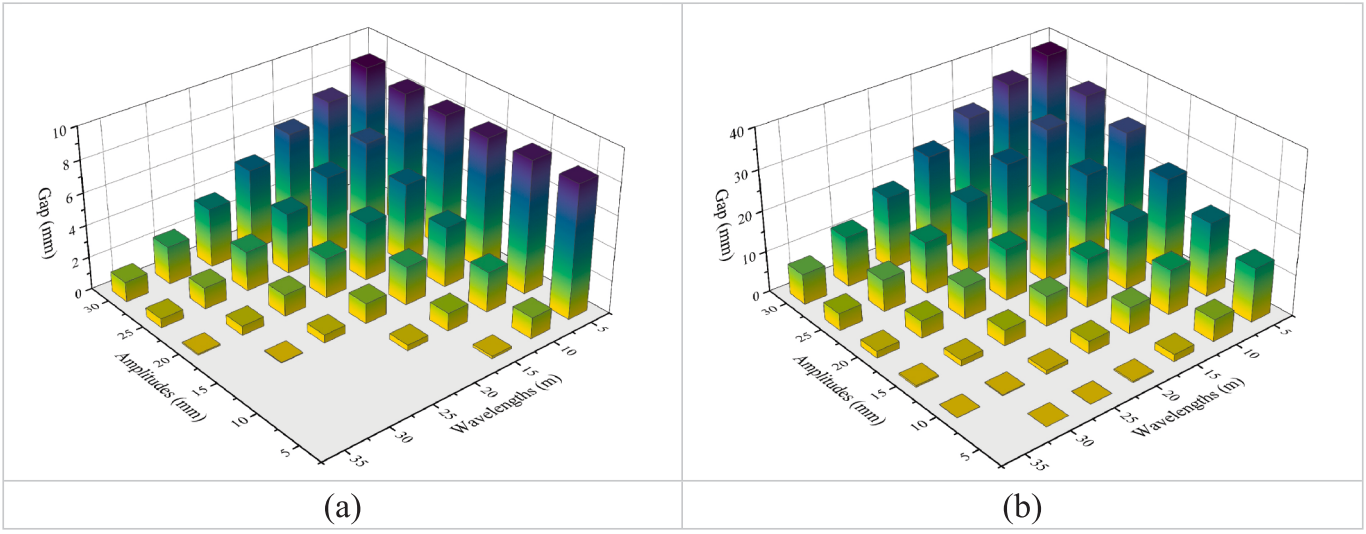


Fig. 15. Maximum gap value between sleeper and ballast of left rail under different scenarios: (a) left rail; and (b) right rail.

force also rises with the increasing amplitude of lateral subgrade settlement. Notably, the lateral wheel-rail contact force of the right rail is greater than that of the left rail, increasing from 6.09 kN to 9.15 kN (i.e., an increase of 50.25%).

Fig. 17 illustrates the variations of vertical and lateral wheel-rail contact forces with settlement wavelength L, under a constant lateral settlement amplitude of 20 mm (Case 7 to Case 12 in Table 1). Overall, the peak wheel-rail contact forces decrease monotonically with increasing wavelength. For example, the peak vertical contact force on the right rail decreases from 123.20 kN at $L = 10$ m to 103.55 kN at $L =$

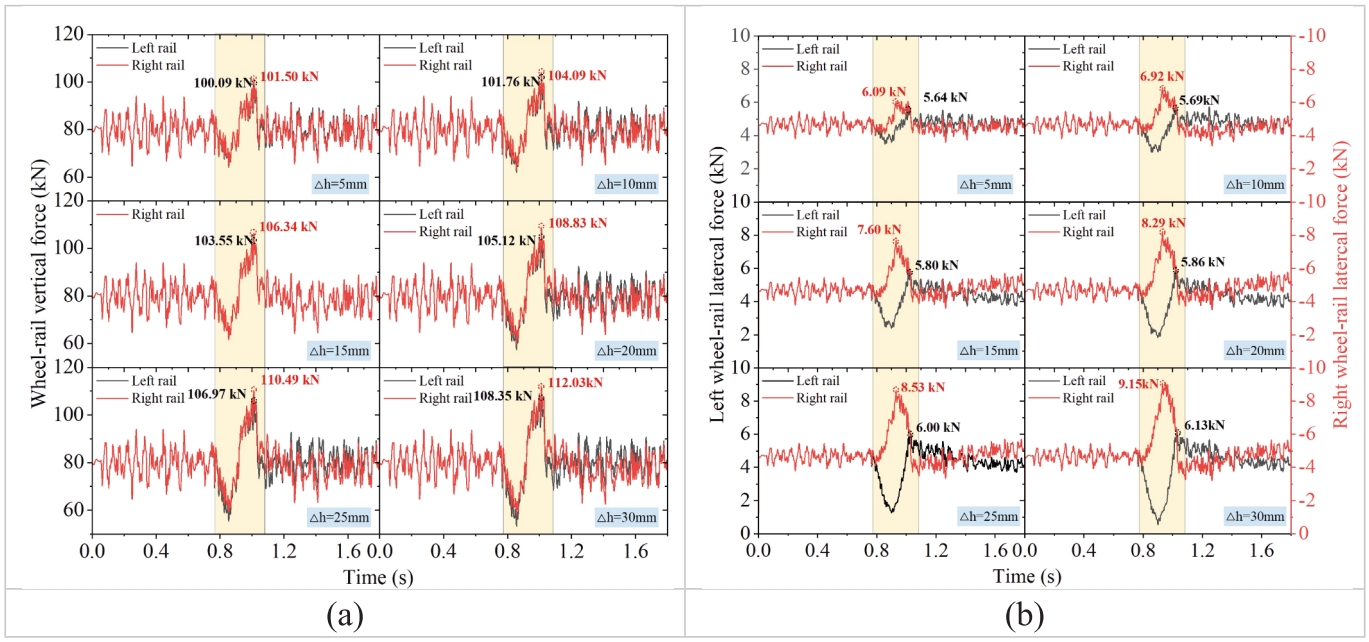


Fig. 16. The time-history curves of wheel-rail contact forces calculated for different combinations of 20-m wavelength and lateral amplitude ranging from 5 mm to 30 mm of differential subgrade settlement: (a) vertical wheel-rail contact forces; and (b) lateral wheel-rail contact forces.

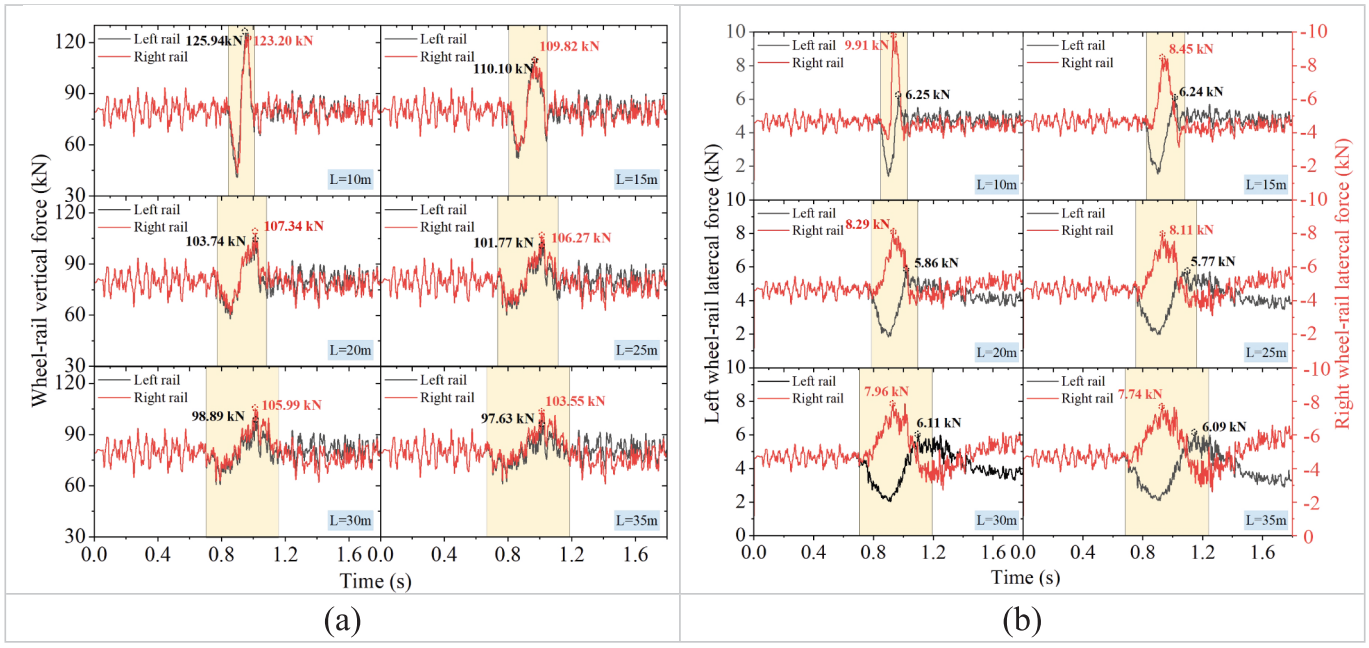


Fig. 17. The time-history curves of wheel-rail contact forces calculated for subgrade settlement wavelength ranging from 10 m to 35 m and the lateral settlement amplitude of 20 mm: (a) the vertical wheel-rail contact force; and (b) the lateral wheel-rail contact force.

35 m, while the corresponding lateral force decreases from 9.91 kN to 7.74 kN. This indicates that short-wavelength differential settlement induces more severe dynamic impact on the wheel-rail interface.

In addition, a pronounced asymmetry between the left and right rails is observed due to the imposed lateral settlement. The lateral contact force on the right rail remains consistently larger than that on the left rail over the entire wavelength range, reflecting the persistent geometric bias and lateral wheel-rail interaction caused by lateral settlement. For the vertical contact force, a load reversal phenomenon occurs: when the settlement wavelength is no greater than 15 m, the left rail experiences larger vertical contact forces due to dominant inertial effects under short-wavelength excitation; in addition, as the wavelength increases, the geometric load redistribution becomes dominant, resulting in larger vertical forces on the right rail. These results suggest that short-wavelength settlement mainly governs dynamic impact amplification, whereas long-wavelength settlement leads to sustained asymmetric load distribution, both of which have important implications for ballasted track performance and maintenance.

The maximum vertical wheel-rail contact force values under different combinations of settlement wavelength and amplitude are plotted in Fig. 18. To ensure safe and comfortable train operation, the limiting values of typical dynamic responses for high-speed trains are

listed in Table 2 [48]. Note that the gray plane in the graph represents the safety limit, with points below the plane considered safe and those above it deemed risky (i.e., the safety limit is exceeded). From Fig. 18, it is evident that as the wavelength decreases and the amplitude increases, the maximum vertical wheel-rail contact force increases dramatically. Particularly, when the wavelength is less than 10 m and the amplitude is greater than 20 mm, the maximum vertical wheel-rail contact force exceeds the specified safety limit. Therefore, the differential subgrade settlement of small wavelength and large amplitude aggravates the wheel-rail contact forces, posing severe impact on both train operation safety and track performance.

Fig. 19 shows the time-history curves of the vertical carbody acceleration (center of gravity). The vertical carbody acceleration exhibits approximately sinusoidal variations with two peaks corresponding to the passages of the front and rear bogies through the settlement area. This pattern indicates that the differential subgrade settlement has a great influence on ride comfort. When the settlement wavelength remains constant, the vertical carbody acceleration increases linearly with increasing lateral settlement amplitude, as shown in Fig. 19(a). Conversely, Fig. 19(b) shows that, for a given lateral settlement amplitude, the vertical carbody acceleration decreases as the wavelength increases from 10 m to 35 m.

Fig. 20 plots the maximum vertical carbody acceleration under different combinations of settlement wavelength and lateral amplitude. As the amplitude increases, the maximum vertical carbody acceleration also increases. However, it is interesting to observe that the maximum vertical carbody acceleration first increases and then decreases with increasing wavelength, reaching its peak around the wavelength of 10 m. This observation may suggest that the suspension system of the vehicle has a certain damping effect on the short-wave rail irregularities. Note that the peak in maximum vertical acceleration of the carbody at a settlement wavelength of approximately 10 m is indeed closely related to the dynamic characteristics of the vehicle-track system. Physically, the settlement wavelength, together with train speed, determines the equivalent excitation frequency of the track irregularity. When this equivalent excitation frequency approaches the lower-order natural frequency range of the vehicle suspension system, the carbody response is significantly amplified. For the vehicle parameters and operating speed used in this study, a settlement wavelength of around 10 m corresponds to an excitation frequency within the sensitive frequency range of the carbody-bogie system, resulting in the maximum vertical acceleration of the carbody. Since this study focused on revealing the influence of spatially differential settlement wavelength on vehicle dynamic response amplitudes through time-domain analysis, no separate frequency-domain analysis was conducted. However, existing literature shows that similar “sensitive wavelength” phenomena are generally associated with the dynamic properties of the vehicle suspension system and vehicle-track coupled vibrational behavior. Therefore, in future research, frequency-domain or time–frequency analysis could be incorporated within the current model framework to further investigate the resonance mechanisms of the vehicle-track coupled system under differential settlement excitation.

Fig. 21 illustrates the time-history variations of the wheel unloading rate calculated for different combinations of wavelength and amplitude. The wheel load exhibits a general pattern of initial reduction followed by an increase as the train passes through the subgrade settlement area. As shown in Fig. 21(a), for a given wavelength, the maximum wheel unloading rate increases linearly with increasing amplitude. In contrast, as shown in Fig. 21(b), for a given amplitude, the wheel unloading rate decreases with increasing wavelength.

Fig. 22 presents the maximum wheel unloading rate under different combinations of settlement wavelength and amplitude. It is worth noting that the points above the gray plane indicate that they exceed the safety limit. As shown in Fig. 22, the maximum wheel unloading rate decreases with increasing wavelength and increases with increasing amplitude. This observation highlights the potential risk of train derailment due to differential subgrade settlement, particularly for cases with small wavelengths and large amplitudes, posing a serious threat to the operational safety of high-speed trains.

Fig. 23 plots the variations of maximum vertical carbody acceleration, maximum lateral carbody acceleration and maximum wheel unloading rate concerning the running speed of the train, for a settlement wavelength of 20 m and a lateral settlement amplitude of 20 mm (Case 4 in Table 1). The graph illustrates that the train's dynamic responses increase approximately linearly with train speed. Notably, when the train speed reaches 300 km/h, the wheel unloading rate surpasses

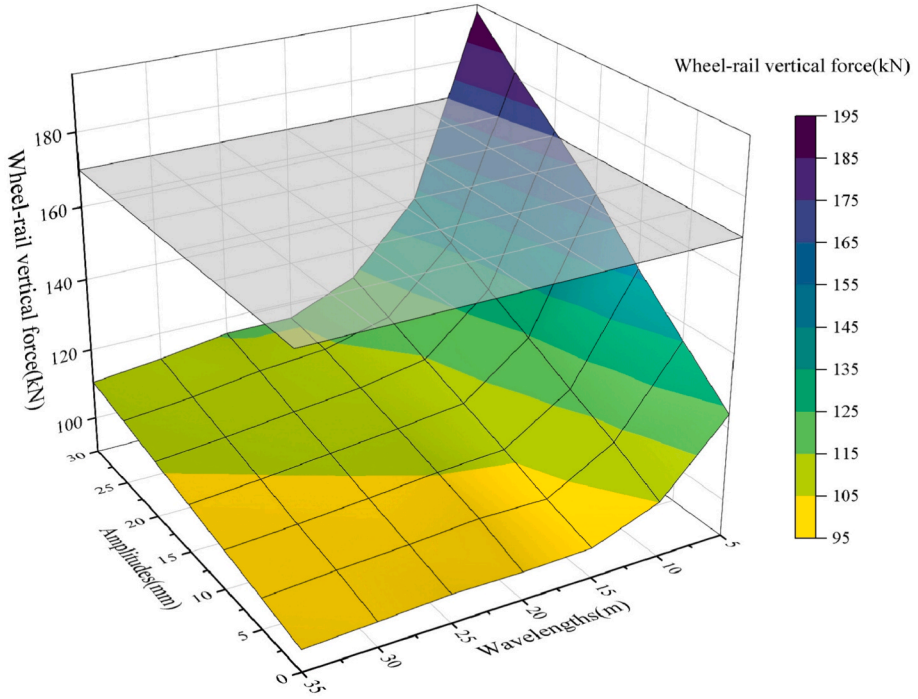


Fig. 18. Maximum vertical wheel-rail contact force calcualted for different amplitude and wavelength combinations of differential subgrade settlement.

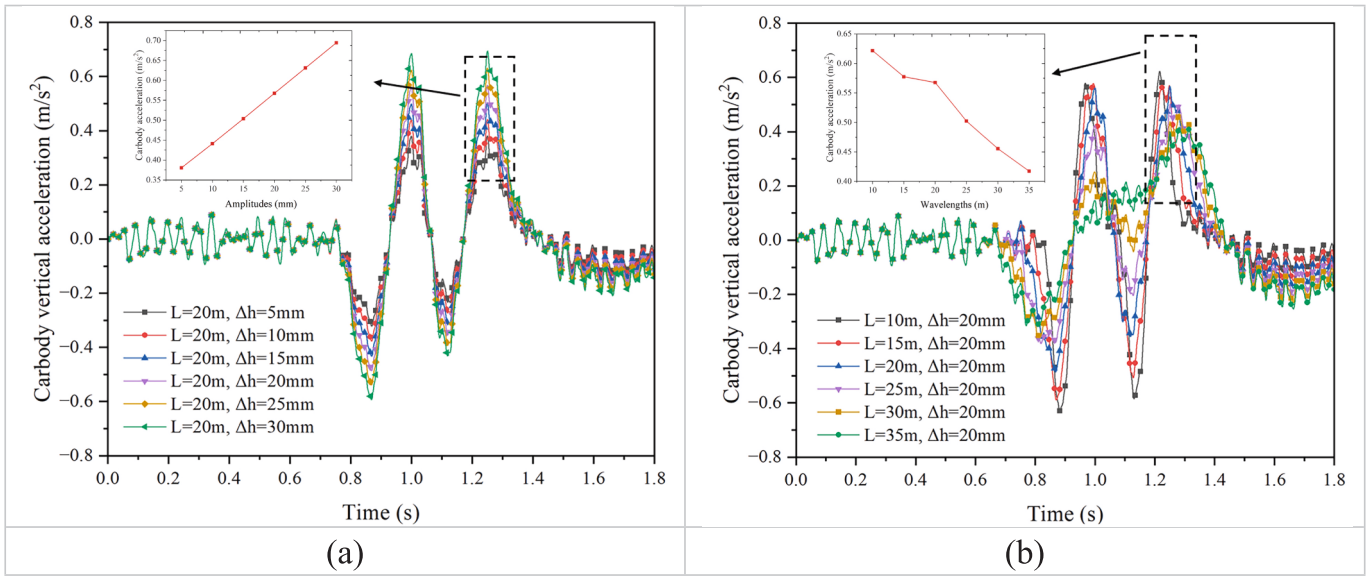


Fig. 19. The time-history curves of vertical carbody acceleration calculated for different wavelength and amplitude combinations of differential subgrade settlement: (a) constant wavelength of 20 m; and (b) constant amplitude of 20 mm.

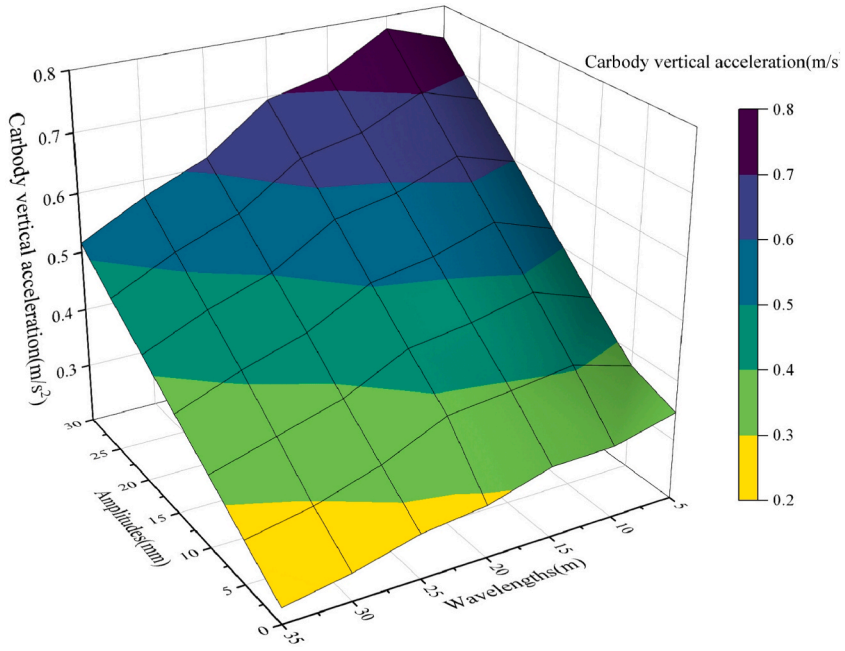


Fig. 20. Maximum vertical carbody acceleration with different amplitude and wavelength combinations of differential subgrade settlement.

the limit values specified in Table 2.

Effect of differential subgrade settlement on fastening forces

Rail fasteners play a crucial role in connecting rails and sleepers, facilitating the transfer of wheel loads from rails to substructures and thus maintaining track geometry regularity [49]. In this study, the rail fasteners were assumed pressurized if the fastening forces are positive, or tensioned otherwise. Fig. 24 shows the spatial–temporal variations of fastening forces for the Case 4 in Table 1.

As shown in Fig. 24, when the train is located in the areas without differential subgrade settlement (at time T = 0.51 s), the peak fastening force induced by train load is 24.87 kN. Besides, under the combined action of settlement and track self-weights, the fastening force of the left rail is −3.35 kN at the settlement boundary area (i.e., the rail fasteners are tensioned), but it is 3.26 kN at the settlement center area (i.e., the rail fasteners are pressurized). In contrast, the fastening force of the right rail is 10.12 kN at the boundary of subgrade settlement area, but is −3.02 kN at the settlement center. This phenomenon is attributed to the upward arching of the left rail at the boundary of settlement area and the compression of the right rail at the boundary, as shown in Fig. 12.

When the wheelset reaches the settlement boundary area (at time T = 0.74 s), the left rail, which previously experienced upwarping displacement, now deforms downwards under the moving wheel loads. Therefore, the left rail fasteners located at the settlement boundary area transition from being tensioned to being pressurized, with the fastening force being 20.03 kN. Conversely, the fastening force of the right rail at the settlement boundary area further increases and reaches the

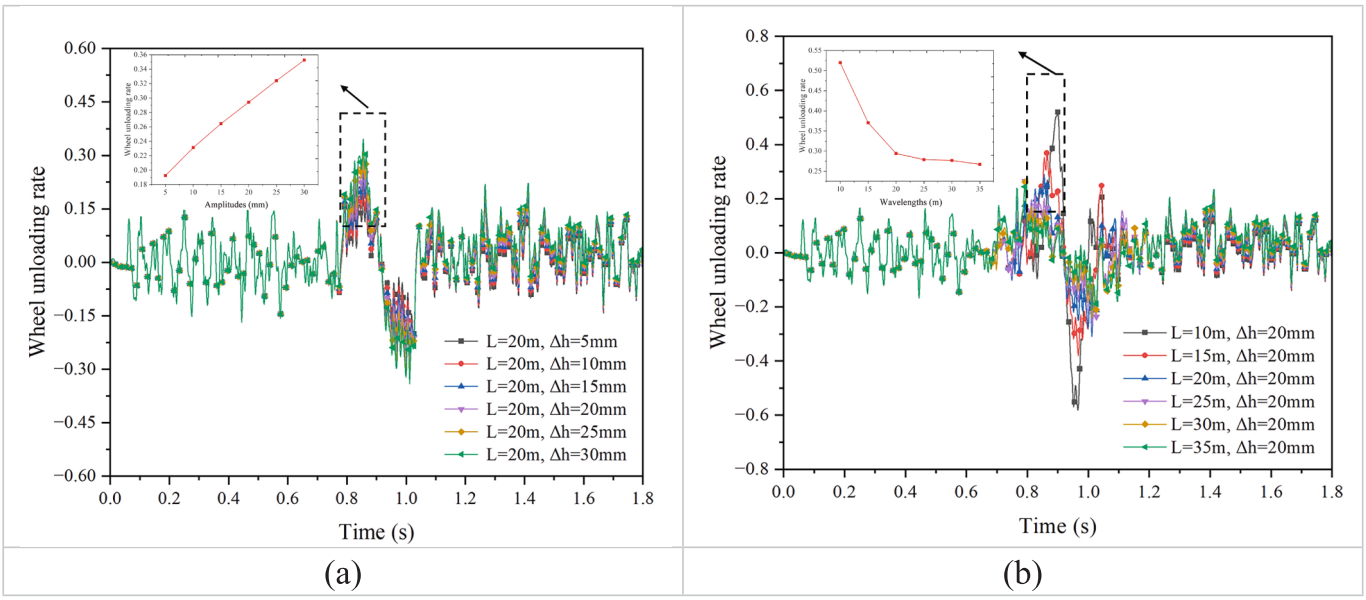


Fig. 21. Time-history variations of the wheel unloading rate calculated for different wavelength and amplitude combinations of differential subgrade settlement: (a) constant wavelength of 20 m; and (b) constant amplitude of 20 mm.

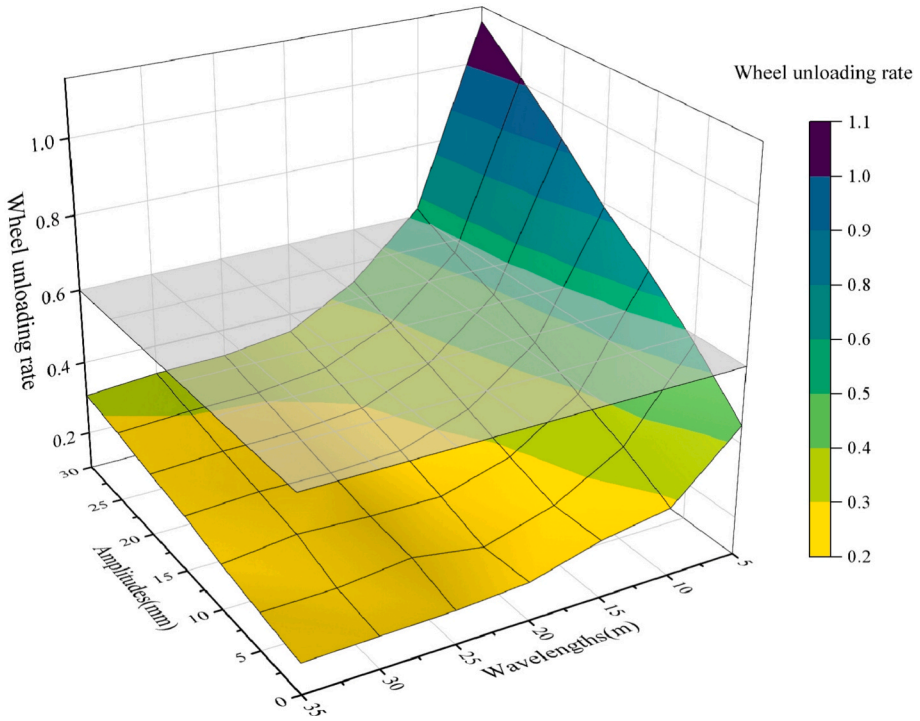


Fig. 22. Maximum wheel unloading rate with different amplitude and wavelength combinations of differential subgrade settlement.

maximum value of 31.07 kN. As the wheelset moves to the center of the subgrade settlement area (at time T = 0.89 s), the fastening force of the left rail reaches the maximum value of 41.59 kN under the train loads. The fasteners of the right rail located in the settlement center area, which were previously tensioned, also become pressurized with the fastening force being 8.75 kN.

Consequently, when the subgrade experiences severe spatially differential settlement, the rail fasteners located near the subgrade settlement area are prone to tension–compression-type fatigue damage. Such spatially differential subgrade settlement leads to a pronounced non-uniform distribution of track support stiffness, thereby altering the bending moment transfer and load redistribution within the track structures. More severely impacted rail fasteners are concentrated in the settlement center on the side with smaller settlement and at the settlement boundary on the side with larger settlement. The former behaves as a relatively stiff support, attracting higher bending moments and wheel-rail loads, whereas the latter acts as a mechanical transition zone with concentrated bending moment gradients. Under moving train loads, this stiffness contrast induces repeated load transfer and stress concentration in these regions, making them more susceptible to structural damage. In summary, abrupt changes in track stiffness leading to discontinuous bending moment transfer, combined with the

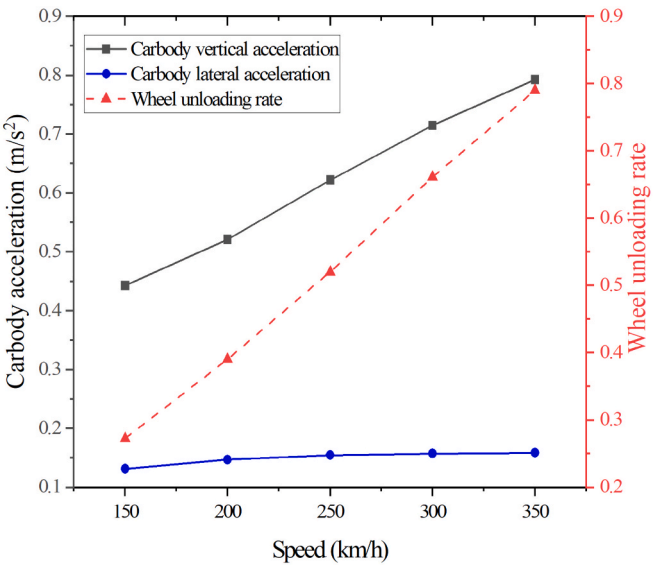


Fig. 23. Variations of maximum carbody acceleration and maximum wheel unloading rate with train speed.

redistribution of wheel-rail loads and subgrade dynamic stress responses, are the primary mechanical mechanisms causing these regions to be more susceptible to damage.

Effect of differential subgrade settlement on dynamic subgrade stress

Based on the analysis results presented above, it is critical to study the influence of differential subgrade settlement on dynamic subgrade responses for long-term, in-service track performance monitoring and control.

Fig. 25 illustrates the distributions of vertical dynamic subgrade stress corresponding to representative locations of the high-speed train. As shown in Fig. 25(c), when the wheelset is located in the non-settlement area, the maximum vertical dynamic stress induced by the train loads is 30.16 kPa, with nearly symmetrical stress distribution on both sides of the subgrade. In Fig. 25(d), as the train wheelset reaches the boundary of the subgrade settlement area, the maximum vertical dynamic stress under the right rail increases to 31.55 kPa, while it is still 29.84 kPa under the left rail. In combination with Fig. 12, this occurs because gaps between the track and subgrade at the settlement boundary on the left side lead to load distribution to adjacent areas, while the right side is squeezed more. As seen in Fig. 25(b), when the wheelset moves to the settlement center area, the maximum vertical dynamic stress under the right rail is 29.95 kPa, while that under the left rail increases dramatically to 49.04 kPa, surpassing the stresses caused by the train loads only. This observation highlights that the lateral differential subgrade settlement causes repeated flapping between the track and subgrade as the train passes by.

Previous studies have indicated that the accumulated vertical plastic deformation of the subgrade soil under the repeated moving train loads is governed by the vertical dynamic stress [50]. The numerical simulation results presented above suggest that severe spatially differential subgrade settlement could generate even much greater vertical dynamic stress in the subgrade, resulting in aggravated plastic deformation and differential subgrade settlement. In particular, the side with smaller settlement suffers greater impact at the settlement center, and the side with greater settlement experiences greater impact at the settlement boundary, leading to larger plastic deformation in these areas. This process accelerates further development of lateral subgrade settlement, which makes the differential subgrade settlement tend to be spatially non-uniform.

Summary and conclusions

This paper established a 3D train-ballasted track-subgrade coupled model that considers spatially differential subgrade settlement, and an iterative method to reveal the relationship between subgrade settlement and track irregularity was developed. On this basis, the dynamic responses of and the interactions between individual components of the coupled system were analyzed. The main conclusions of this paper are summarized as follows.

(1) Severe spatial differential subgrade settlement leads to unsupported sleepers in the settlement area due to the high bending stiffness of the rails. The smaller settlement wavelengths and larger settlement amplitudes result in greater gaps between the track and subgrade.
(2) The wheel-rail interaction is intensified in the subgrade settlement area, showing a distinct pattern of initial wheel load reduction and subsequent wheel load increase. Both maximum wheel-rail contact force and wheel unloading rate increase with decreasing wavelength and increasing amplitude, seriously affecting the driving safety. It is worth noting that the vertical

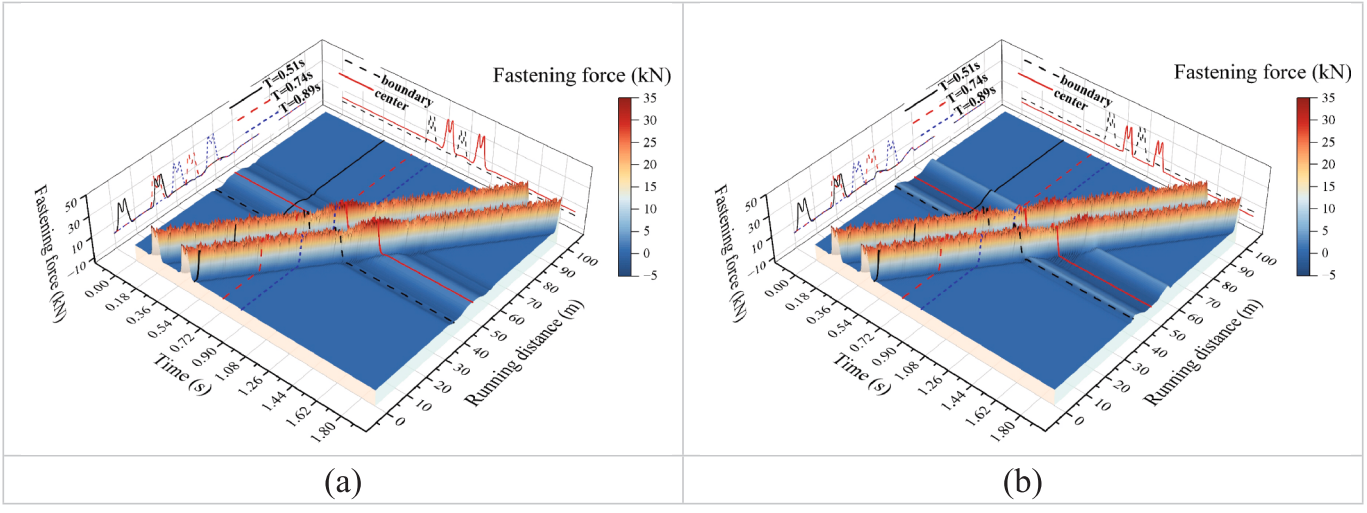


Fig. 24. The spatial–temporal variations of fastening forces due to lateral differential subgrade settlement: (a) the left rail (the side with less settlement); and (b) the right rail (the side with greater settlement).

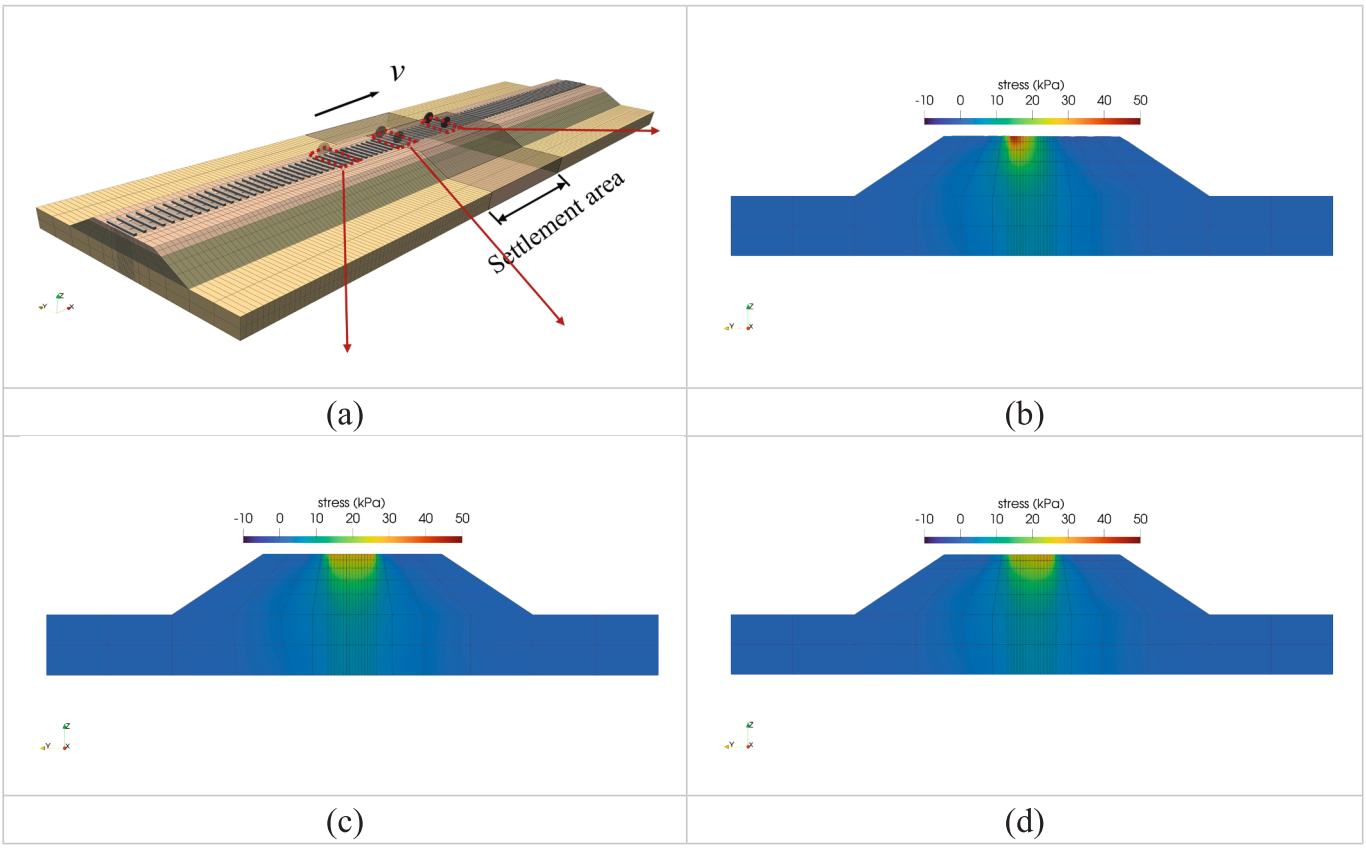


Fig. 25. Distribution contours of vertical dynamic subgrade stress under moving train loads: (a) diagram of the track-subgrade coupled model; (b) the train is located at the settlement center; (c) the train is located at the non-settlement area; and (d) the train is located at the settlement edge.

wheel-rail contact force is greater on the side with less settlement when the settlement wavelength is no more than 15 m, as well as on the side with larger settlement when the settlement wavelength is greater than 15 m.

(3) The maximum vertical carbody acceleration increases with increasing settlement amplitude. However, it first increases and then decreases with increasing wavelength. There exists a sensitive wavelength of around 10 m in terms of running safety and ride comfort, indicating that the train suspension system can effectively reduce vibration and improve ride comfort in short-wave irregularities.

(4) Due to the combined effects of spatial differential subgrade settlement and moving train loads, the rail fastening forces are greater in the settlement center area on the side with less settlement, as well as in the settlement boundary on the side with greater settlement. It thus seriously affects the durability of the track structures. Additionally, during the train passage through the subgrade settlement area, the track impacts the subgrade repeatedly, intensifying the uneven spatial distribution of dynamic subgrade stress and further aggravating the development of differential subgrade settlement.

Future work may further enhance the present model by improving its engineering applicability and deepening physical insights. This includes incorporating more refined material constitutive models to capture micro-scale mechanical behavior and structural degradation under dynamic loading, as well as establishing a two-way coupled framework between settlement evolution and dynamic responses to predict the long-term development of differential subgrade settlement. Multi-scale approaches could also be introduced to account for ballast particle compaction and re-support behavior under long-term cyclic loading. Furthermore, systematic validation using field monitoring data is needed to correlate non-intuitive damage patterns, such as stress concentrations in stiffness-transition and off-center regions, with actual track and subgrade defects, providing a reliable mechanical basis for identifying hidden subgrade failures and optimizing maintenance strategies based on vehicle–track dynamic responses.

CRediT authorship contribution statement

Yuanjie Xiao: Writing – review & editing, Writing – original draft, Validation, Supervision, Resources, Project administration, Methodology, Investigation, Funding acquisition, Formal analysis, Conceptualization. **Zixuan Deng:** Writing – review & editing, Writing – original draft, Visualization, Validation, Software, Methodology, Investigation, Formal analysis, Data curation, Conceptualization. **Sijia Zhou:** Writing – review & editing, Writing – original draft, Visualization, Validation, Software, Methodology, Investigation, Formal analysis, Data curation, Conceptualization. **Zhenxing Chang:** Writing – review & editing, Software, Methodology, Conceptualization. **Jianfeng Mao:** Writing – review & editing, Supervision, Software, Resources, Methodology, Investigation, Formal analysis, Conceptualization. **Zehan Shen:** Writing – review & editing, Validation, Software, Methodology, Investigation, Conceptualization. **Weidong Wang:** Writing – review & editing, Supervision, Resources, Project administration, Methodology, Investigation, Funding acquisition, Conceptualization. **Sui Tan:** Writing – review & editing, Resources, Project administration, Conceptualization.

Declaration of competing interest

The authors declare that they have no known competing financial interests or personal relationships that could have appeared to influence

the work reported in this paper.

Acknowledgements

This work was jointly supported by the Science and Technology Research and Development Program Project of China Railway Group Limited (Practical technology 2023-Special-07), the Science Fund for Distinguished Young Scholars of Hunan Province, China (2024JJ2073), and the National Natural Science Foundation of China (52578542, 52178443). The computing resources provided by the High-Performance Computing Center of Central South University are gratefully acknowledged.

Appendix I

Table A1
Input parameters of the vehicle model.

Parameter	Value
Mass of carbody, M_c	4.8×10^4 kg
Roll mass moment of carbody, J_{cx}	1.15×10^5 kg·m^2
Pitch mass moment of carbody, J_{cy}	2.7×10^6 kg·m^2
Yaw mass moment of carbody, J_{cz}	2.7×10^6 kg·m^2
Mass of bogie, M_t	3.2×10^3 kg
Roll mass moment of bogie, J_{tx}	3.2×10^3 kg·m^2
Pitch mass moment of bogie, J_{ty}	7.2×10^3 kg·m^2
Yaw mass moment of bogie, J_{tz}	6.8×10^3 kg·m^2
Mass of wheelset, M_w	2.4×10^3 kg
Roll mass moment of wheelset, J_{wx}	1.2×10^3 kg·m^2
Yaw mass moment of wheelset, J_{wz}	1.2×10^3 kg·m^2
Axle load	15 t
Velocity	250 km/h
Longitudinal secondary suspension stiffness, K_{sx}	2.4×10^5 N/m
Lateral secondary suspension stiffness, K_{sy}	4.8×10^5 N/m
Vertical secondary suspension stiffness, K_{sz}	4.0×10^5 N/m
Longitudinal secondary suspension damping, C_{sx}	1.2×10^5 N·s/m
Lateral secondary suspension damping, C_{sy}	3.0×10^4 N·s/m
Vertical secondary suspension damping, C_{sz}	6.0×10^4 N·s/m
Longitudinal primary suspension stiffness, K_{px}	9.0×10^6 N/m
Lateral primary suspension stiffness, K_{py}	3.0×10^6 N/m
Vertical primary suspension stiffness, K_{pz}	1.04×10^6 N/m
Longitudinal primary suspension damping, C_{px}	0 N·s/m
Lateral primary suspension damping, C_{py}	0 N·s/m
Vertical primary suspension damping, C_{pz}	5.0×10^4 N·s/m

Table A2
Input parameters of the FEM model for the ballasted track system.

Parameter	Value
Elastic modulus of rail, E	205.9 GPa
Inertia moment around the y axis of rail, I_y	3.217×10^{-5} m^4
Inertia moment around the z axis of rail, I_z	5.24×10^{-6} m^4
Mass of sleeper, M_{sl}	375 kg
Fastener stiffness, K_{fx}, K_{fy}, K_{fz}	29.4, 29.4, 80 MN·m^{-1}
Fastener damping, C_{fx}, C_{fy}, C_{fz}	5.2×10^4, 5.2×10^4, 5×10^4 N·s·m^{-1}
Sleeper spacing	0.625 m
Longitudinal shear stiffness	78.4 MN·m^{-1}
Lateral shear stiffness	78.4 MN·m^{-1}
Longitudinal shear damping	80 kN·s·m^{-1}
Lateral shear damping	80 kN·s·m^{-1}
Thickness of ballast layer	0.35 m
Density of ballast layer	1800 kg·m^{-3}
Elastic modulus of top embankment, E_t	200 MPa
Poisson's ratio of top embankment, μ_t	0.3
Density of top embankment, ρ_t	2360 kg·m^{-3}
Elastic modulus of bottom embankment, E_b	150 MPa
Poisson's ratio of bottom embankment, μ_b	0.3
Density of bottom embankment, ρ_b	2340 kg·m^{-3}
Elastic modulus of subgrade, E_s	60 MPa
Poisson's ratio of subgrade, μ_s	0.3
Density of subgrade, ρ_s	2300 kg·m^{-3}

Data availability

Data will be made available on request.

References

[1] Guo L, Wang J, Cai Y, Liu H, Gao Y, Sun H. Undrained deformation behavior of saturated soft clay under long-term cyclic loading. Soil Dyn Earthq Eng 2013;50:28–37. https://doi.org/10.1016/j.soildyn.2013.01.029.

[2] Liu J, Xiao J. Experimental Study on the Stability of Railroad Silt Subgrade with increasing Train speed. J Geotech Geoenvironmental Eng 2010;136:833–41. https://doi.org/10.1061/(ASCE)GT.1943-5606.0000282.

[3] Puppala AJ, Mohammad LN, Allen A. Permanent deformation characterization of subgrade soils from RLT test. J Mater Civ Eng 1999;11:274–82. https://doi.org/10.1061/(ASCE)0899-1561(1999)11:4(274).

[4] Yang Z, Yue Z, Tai B. Investigation of the deformation and strength properties of fouled graded macadam materials in heavy-haul railway subgrade beds. Constr Build Mater 2021;273:121778. https://doi.org/10.1016/j.conbuildmat.2020.121778.

[5] Li Z, Xu L, Wang W, Du X, Yu Z, Liu P, et al. Study on the prediction of the cumulative deformation of high-speecrailway subgrade under the cyclic dynamic loads of vehicle. Journal of Railway Science and Engineering 2024;21(04):1445–56.

[6] Zhang Q. Study of Doubleblock ballastless trackcausing by subgrade differential settlement. Southwest Jiaotong university 2007.

[7] Kaewunruen S, Chiengson C. Railway track inspection and maintenance priorities due to dynamic coupling effects of dipped rails and differential track settlements. Eng Fail Anal 2018;93:157–71. https://doi.org/10.1016/j.engfailanal.2018.07.009.

[8] Dahlberg T. Some railroad settlement models - a critical review. Proc Inst Mech Eng Part F-J Rail Rapid Transit 2001;215:289–300. https://doi.org/10.1243/0954409011531585.

[9] Lundqvist A, Dahlberg T. Load impact on railway track due to unsupported sleepers. Proc Inst Mech Eng Part F-J Rail Rapid Transit 2005;219:67–77. https://doi.org/10.1243/095440905X8790.

[10] Cai X, Liu W, Wang P, Ning X. Effect of land subsidence on regularity of double-block ballastless track. Eng Mech 2014;31:160–5.

[11] Chen Z, Zhai W, Cai C, Sun Y. Safety threshold of high-speed railway pier settlement based on train-track-bridge dynamic interaction. Sci China-Technol Sci 2015;58:202–10. https://doi.org/10.1007/s11431-014-5692-0.

[12] Zhou W, Nie L, Jiang L, Feng Y, Tan Z, Chai X. Mapping relation between pier settlement and rail deformation of unit slab track system. Structures 2020;27:1066–74. https://doi.org/10.1016/j.istruc.2020.07.023.

[13] Zou C, Zhou S, Wang B, Wei K. Model test study of influence of differential subgrade settlement on ballasted track settlement. J Tongji Univ 2011;39:862–9.

[14] Zhang S, Mao X, Wen Z, Jin X. Effect of unsupported sleepers on wheel/rail normal load. Soil Dyn Earthq Eng 2008;28:662–73. https://doi.org/10.1016/j.soildyn.2007.08.006.

[15] Zhu JJ, Ahmed AKW, Rakheja S, Khajepour A. Development of a vehicle-track model assembly and numerical method for simulation of wheel-rail dynamic interaction due to unsupported sleepers. Veh Syst Dyn 2010;48:1535–52. https://doi.org/10.1080/00423110903540751.

[16] Shi J, Chan AH, Burrow MPN. Influence of unsupported sleepers on the dynamic response of a heavy haul railway embankment. Proc Inst Mech Eng Part F-J Rail Rapid Transit 2013;227:657–67. https://doi.org/10.1177/0954409713495016.

[17] Zakeri JA, Fattahi M, Ghanimoghadam MM. Influence of unsupported and partially supported sleepers on dynamic responses of train-track interaction. J Mech Sci Technol 2015;29:2289–95. https://doi.org/10.1007/s12206-015-0521-3.

[18] Nielsen JCO, Li X. Railway track geometry degradation due to differential settlement of ballast/subgrade - Numerical prediction by an iterative procedure. J Sound Vib 2018;412:441–56. https://doi.org/10.1016/j.jsv.2017.10.005.

[19] Varandas JN, Holscher P, Silva MAG. Settlement of ballasted track under traffic loading: Application to transition zones. Proc Inst Mech Eng Part F-J Rail Rapid Transit 2014;228:242–59. https://doi.org/10.1177/0954409712471610.

[20] Wang H, Markine V. Dynamic behaviour of the track in transitions zones considering the differential settlement. J Sound Vib 2019;459:114863. https://doi.org/10.1016/j.jsv.2019.114863.

[21] Varandas JN, Holscher P, Silva MAG. Dynamic behaviour of railway tracks on transitions zones. Comput Struct 2011;89:1468–79. https://doi.org/10.1016/j.compstruc.2011.02.013.

[22] Grassie SL, Cox SJ. The Dynamic Response of Railway Track with Unsupported Sleepers. Arch Proc Inst Mech Eng Part Transp Eng 1984–1988 198–202(199), 1985,:123–36. https://doi.org/10.1243/pime_proc_1985_199_149_01.

[23] Paixao A, Fortunato E, Calcada R. The effect of differential settlements on the dynamic response of the train-track system: a numerical study. Eng Struct 2015;88:216–24. https://doi.org/10.1016/j.engstruct.2015.01.044.

[24] Varandas JN, Paixao A, Fortunato E. A study on the dynamic train-track interaction over cut-fill transitions on buried culverts. Comput Struct 2017;189:49–61. https://doi.org/10.1016/j.compstruc.2017.04.017.

[25] Zhang X, Burrow M, Zhou S. An investigation of subgrade differential settlement on the dynamic response of the vehicle-track system. Proc Inst Mech Eng Part F-J Rail Rapid Transit 2016;230:1760–73. https://doi.org/10.1177/0954409715613538.

[26] Sun Y, Guo Y, Chen Z, Zhai W. Effect of Differential Ballast Settlement on Dynamic Response of Vehicle-Track coupled Systems. Int J Struct Stab Dyn 2018;18:1850091. https://doi.org/10.1142/S0219455418500918.

[27] Jiang H, Li X, Xin G, Yao Z, Zhang J, Liang M. Geometry mapping and additional stresses of ballastless track structure caused by subgrade differential settlement under self-weight loads in high-speed railways. Transp Geotech 2019;18:103–10. https://doi.org/10.1016/j.trgeo.2018.10.007.

[28] Tan J, Liu W, Wang Z, Ran W, Cui Y, Cui Z. Grading evaluation method for uneven subgrade settlement of high-speed railway based on a temporal multi-task network [J]. Transp Geotech 2025:101819.

[29] Xu W, Guo Y, You M. Intelligent identification of differential subgrade settlement of ballastless track system based on vehicle dynamic responses and 1D-CNN approach[J]. Transp Geotech 2024;48:101302.

[30] Xiao F, Shan Y, Zhou G, Lin W, Li J. Critical transverse differential settlement between modern tram pile-plank-supported subgrade and surrounding pavement subgrade[J]. Transp Geotech 2023;38:100896.

[31] Jiang H, Li X, Xin G, Yao Z, Zhang J, Liang M. Geometry mapping and additional stresses of ballastless track structure caused by subgrade differential settlement under self-weight loads in high-speed railways[J]. Transp Geotech 2019;18:103–10.

[32] Fan YS, Mao XS, Meng QM, Luo BB. The Numerical simulation of the Lateral Inhomogeneous Deformation of the Permafrost Subgrade. Adv Mater Res 2014;945–949:198–202. https://doi.org/10.4028/www.scientific.net/AMR.945-949.198.

[33] Cui X, Guo G, Du B, Cai X, Zhou R. Effects of lateral differential settlement of the subgrade on deformation behavior and damage evolution of CRTS II slab track. Eng Fail Anal 2021;129:105674. https://doi.org/10.1016/j.engfailanal.2021.105674.

[34] Zhang K, Zhang X, Zhou S. Influence of Lateral Differential Settlement of Subgrade on Dynamic Performance of High-speed Vehicle System. J Eng Mech 2022;148:04022008. https://doi.org/10.1061/(ASCE)EM.1943-7889.0002065.

[35] G. Li, H. Li, L. Ma, S. Wu, D. Li, Q. Gao, X. Zhang. Influence of transverse differential settlement deformation of subgradeon vehicle-rail dynamic response, Journal of Vibration Engineering, 1-12.

[36] Zhai W. Vehicle-track coupling dynamics. fourth edition. China: Science Press, Beijing; 2015.

[37] Cai X, Tan S, Shen Y, Cai X. Dynamic analysis of laying elastic sleeper on ballast track in tunnel. Journal of the China Railway Society 2018;40(01):87–93.

[38] Mao J, Xiao Y, Yu Z, Tutumluer E, Zhu Z. Probabilistic model and analysis of coupled train-ballasted track-subgrade system with uncertain structural parameters. J Cent South Univ 2021;28(7):2238–56. https://doi.org/10.1007/s11771-021-4765-z.

[39] Wang W, Chen C, Xiao J, Yang C, Xiong H. Research on mechanical characteristics of railway ballast bed based onMicro-mechanical Model. Journal of the China Railway Society 2024;46(06):129–37.

[40] Moreno GA, López AA, García CGM, Ignacio JT, Aguilar JJR. A novel application of computational contact tools on nonlinear finite element analysis to predict ground-borne vibrations generated by trains in ballasted tracks. Modelling 2024;5(4):1454–68.

[41] Code for Design of High-Speed Railway. China Railway Publishing House: Beijing, China, TB10621-2014, 2014.

[42] Liu J, Gu Y, Du Y. Consistent viscous-spring artificial boundaries and viscous-sprinoboundary elements. Chinese Journal of Geotechnical Engineering 2006;09:1070–5.

[43] Zhao G. Calculation model of ballastless track and subgrade deformation on highspeed railway. China Railway Science 2016;37(04):1–8.

[44] Xiang J, Lin S, Yu C, Yuan C, Su W. Transfer rules and effect of stress and deformation of ballastless trackunder uneven subgrade settlement. Journal of Traffic and Transportation Engineering 2019;19(02):69–81.

[45] Zhong Y, Ma C, Gao L, Cai X, Zhao W. Theoretical research on evaluation index of unevensettlement of ballastless track subgradebased on vehicle response. Engineering Mechanics 2021;38(12):147–57.

[46] Xu Q, Li B, Zhou Z. Study on the limited value for the uneven settlement of subgrade undercrts- i type slab track. China Railway Science 2012;33(02):1–6.

[47] Luo Q, Fu H, Liu K, Wang T, Feng G. Monitoring of train-induced responses at asphalt support layer of a high-speed ballasted track. Constr Build Mater 2021;298:123909. https://doi.org/10.1016/j.conbuildmat.2021.123909.

[48] Technical Specification for Dynamic Acceptance of High-speed Railway Engineering. China Railway Publishing House: Beijing, China, TB 10761-2013. 2013.

[49] Xiao Y, Chang Z, Mao J, Zhou S, Wang X, Wang W, et al. Evaluating the effect of rail fastener failure on dynamic responses of train-ballasted track-subgrade coupling system for smart track condition assessment. Materials 2022;15:2675. https://doi.org/10.3390/ma15072675.

[50] Li D, Selig ET. Cumulative plastic deformation for fine-grained subgrade soils. J Geotech Eng 1996;122:1006–13. https://doi.org/10.1061/(ASCE)0733-9410(1996)122:12(1006).

[51] Xiao Y, Zhou S, Chang Z, Mao J, Hua W, Xu B, et al. Analysis of influence of differential subgrade settlement on dynamic responses of the three-dimensional train- ballasted track- subgrade coupled system[J]. Journal of Central South University (Science and Technology) 2023;54(12):4763–76.